Evolution of plastic deformation behavior upon strain-path changes in an A6022-T4 Al alloy sheet

Takayuki HAMA*1
Shogo YAGI*1
Koji TATSUKAWA*1
Yasuhiro MAEDA*2
Yasushi MAEDA*2
Hirohiko TAKUDA*1

*1 Graduate School of Energy Science, Kyoto University, Yoshida-honmachi, Sakyo-ku, Kyoto 606-8501, Japan
*2 Materials Research Laboratory, Technical Development Group, KOBE STEEL, LTD.
1-5-5 Takatsukadai, Nishi-ku, Kobe, HYOGO 651-2271 JAPAN

Corresponding author: Takayuki HAMA (hama@energy.kyoto-u.ac.jp)

Keywords: Al alloy sheet; crystal plasticity finite-element method; biaxial tension; strain-path change; plastic flow; strain rate sensitivity

Highlights

* The evolution of plastic flow after strain-path changes is measured experimentally under various strain paths in an A6022-T4 Al alloy sheet.
* After abrupt change, the plastic work increment of 4.0 $\mathrm{MJ \cdot m^{-3}}$ is necessary before the plastic flow can be represented by the associated flow rule again.
* The temporal deviation from the associated flow rule after abrupt change occurs because the stress ratio cannot follow the change of the direction of plastic strain rate.
* Eventual plastic flow is the same regardless of path change if the final strain paths are identical.

Abstract

The plastic deformation behavior under various strain-path changes in an A6022-T4 Al alloy sheet was studied, focusing on the evolution of the direction of the plastic strain rate θ and the stress ratio φ after abrupt strain-path changes. A cruciform specimen was used to measure the evolution of the plastic deformation behavior after abrupt strain-path change experimentally. Before the strain-path change, the deformation was represented well by the associated flow rule with the Yld2000-2d yield function and isotropic hardening assumption. After the abrupt path change, the deformation temporarily deviated from the associated flow rule, and it could be represented again by the associated flow rule after the plastic work increased roughly 4.0 $\mathrm{MJ \cdot m^{-3}}$, which corresponded to the strain increment of approximately 0.024 under uniaxial tension in the rolling direction. The transitions of θ and φ as a function of plastic work showed that both θ and φ tend to converge to certain values regardless of the strain path if the final strain-path angles are identical. It was also found that the relationships between φ and θ temporarily deviate from the associated flow rule immediately after the abrupt path changes because φ cannot follow the rapid change of θ. Crystal plasticity finite-element simulations reproduced the qualitative tendencies observed in the experiments, but the deviations from the associated flow rule were much more pronounced. Parametric studies showed that φ tends to converge to different values depending on the strain rate sensitivity, whereas θ tends to converge to a same value irrespective of the rate sensitivity exponent. The rate sensitivity exponent $m = 0.044$ gave the best fits with the experimental results in terms of the evolution of both θ and φ under an abrupt change path, although the rate sensitivity exponent determined from macroscopic strass-strain curves were $m = 0.002$.

1. Introduction

The weight reduction of automobiles is greatly needed to reduce CO_2 emissions (Hirsch, 2011); therefore, the demand for lightweight sheet metals, including Al and Mg alloy sheets, has been increasing. However, because the formability of these lightweight materials is notably different from that of conventional steel sheets, finite-element method forming simulations are essential to help determine the optimal forming conditions.

In sheet metal forming simulations, although recently nonassociated flow rules and nonnormality modeling have been actively studied (e.g., Stoughton, 2002; Stoughton and Yoon, 2004, 2009; Cvitanić, et al., 2008; Taherizadeh et al., 2010; Safaei et al., 2014; Lee et al., 2017), the associated flow rule is still often used to represent the plastic deformation behavior of sheet metals for industrial applications. Past studies have shown that the associated flow rule is applicable to reproduce the plastic flow of some materials under linear loading paths, including a brass tube (Hill et al., 1994), a cold-rolled steel sheet (Kuwabara et al., 1998), and an A5154-H112 extruded tube (Kuwabara et al., 2005). In contrast, some studies also reported that the associated flow rule was not applicable when abrupt strain-path changes were involved. For example, Kuroda and Tvergaard (1999) conducted crystal plasticity simulations of abrupt strain-path change tests and showed that the direction of the plastic strain rate after the strain-path change deviated greatly from the normal to the yield surface identified using an abrupt strain-path change test. An abrupt strain-path change test was also conducted experimentally for 6000 series Al alloy and SPCE sheets by Kuwabara et al. (2000) and a pure titanium sheet by Kuwabara et al. (2008) using a cruciform specimen. They also observed a large deviation in the direction of the plastic strain rate from the normal to the contours of equal plastic work.

Because strain-path changes or instantaneous changes of the deformation mode often occur during sheet metal forming processes (Ito, 2005), to perform reliable simulations of metal forming processes, it is vital to understand the plastic flow behavior under a variety of loading paths in detail and to incorporate the characteristics into material modeling. To this end, some quantitative studies were conducted both experimentally and numerically. Yoshida (2017) carried out crystal plasticity simulations to investigate the plastic flow behavior under linear and nonlinear loading paths. By comparing the direction of the plastic strain rate at the same stress state between the linear and nonlinear loading paths, it was concluded that the direction of the plastic strain rate depended on not only the stress state but also the direction of the strain rate. A phenomenological flow rule was also proposed that considered these behaviors. Yoshida and Tsuchimoto (2018) conducted experiments on tension–torsion combined loadings under linear and nonlinear strain paths using pure Al (A1050-O) and ultralow carbon steel tubes. The experimental observations were consistent with those obtained from the abovementioned crystal plasticity simulations and with the results reported by Phillips and Lu (1984) in which 1100-O Al was subjected to tension–torsion tests. They also improved Yoshida's pseudo-corner model (Yoshida, 2017) to obtain better agreement with the experimental results. Recently, Yoshida and Okada (2020) performed similar experiments over a large strain range and examined the effect of the magnitude of the plastic strain at the change of the loading direction on the plastic flow after the path change, showing that the effect of the magnitude of the plastic strain was negligible. They also conducted crystal plasticity simulations and showed that the latent and kinematic hardening of slip systems did not affect the plastic flow after the path change. Yang and Balan (2019) performed simulations of abrupt strain-path change tests using an elasto-viscoplastic phenomenological model with the associated flow rule. They showed that the viscosity resulted in an apparent vertex, although the direction of the plastic strain rate was always normal to the stress path both before and after strain-path changes. They also showed that kinematic hardening and elasticity could also affect the deformation behavior after strain-path changes, even when the normality rule was assumed in the viscoplastic constitutive model.

Most of the past studies focused their attention on the instantaneous plastic flow behavior at the change of strain paths, including the vertex on the yield surface (e.g., Kuroda and Tvergaard, 1999; Kuwabara et al., 2000; Kuroda and Tvergaard, 2001; Kuwabara et al., 2008) and the direction of plastic strain rate immediately after strain-path changes (e.g., Yoshida, 2017; Yoshida and Tsuchimoto, 2018; Yang and Balan, 2019). It has been understood from the past studies that the nonnormality occurs just after abrupt strain path changes because of instability at the strain-path change point, and it tends to disappear as the plastic deformation progresses. Kuroda and Tvergaard (1999) showed from their crystal plasticity simulations of abrupt strain-path change tests of single crystals that the direction of plastic strain rate changed quickly immediately after the abrupt change and then it became completely normal to the stress path. Yang and Balan (2019) examined the evolution of the direction of viscoplastic strain rate after abrupt path changes and showed that after a slight progress in plastic deformation the direction of viscoplastic strain rate tended to converge to fulfill the associated flow rule again. However, most of these results were numerical, and experimental results of further evolution of the plastic flow behavior after abrupt strain-path change have hardly been reported. Particularly, the amount of plastic strain increment which is necessary before convergence is not understood. Yoshida and Okada (2020) studied the plastic flow behavior for a wide range of strains before abrupt strain-path change, but the evolution after abrupt strain-path change to large strains was not examined. Indeed, because strain-path changes frequently occur during press forming of sheet metals and, moreover, plastic instability, including necking, often arises at large strains, it would be significant to study the plastic flow behavior over a large strain range both before and after path changes. Thus, it is important to study further the evolution of the plastic flow behavior after abrupt strain path changes experimentally and the applicability of the associated flow rule for practical purposes.

For these reasons, in the present study, experiments of biaxial tensile tests of an A6022-T4 Al alloy sheet were performed under various linear and nonlinear strain paths. The tests were conducted within the first quadrant of the stress space until the plastic flow roughly converged to a certain state or fracture occurred. Then, the evolution and convergence of the plastic flow behavior was investigated especially focusing on abrupt strain-path change tests. The applicability of the associated flow rule was also discussed from the practical viewpoint. Cruciform specimens were used for this purpose.

Crystal plasticity finite-element simulations were also conducted to analyze the plastic flow behavior from the microscopic as well as theoretical perspectives.

2. Experimental Methods

2.1. Material

The material used in this study was a commercially available 6000 series Al alloy A6022-T4 sheet with 1.0-mm thickness. **Figs. 1(a)** and **(b)** show the inverse pole figure map and pole figures, respectively, obtained from electron backscatter diffraction (EBSD) measurements. The average grain diameter was approximately 43.9 μm. Strong cube components appeared.

2.2. Experimental Procedures

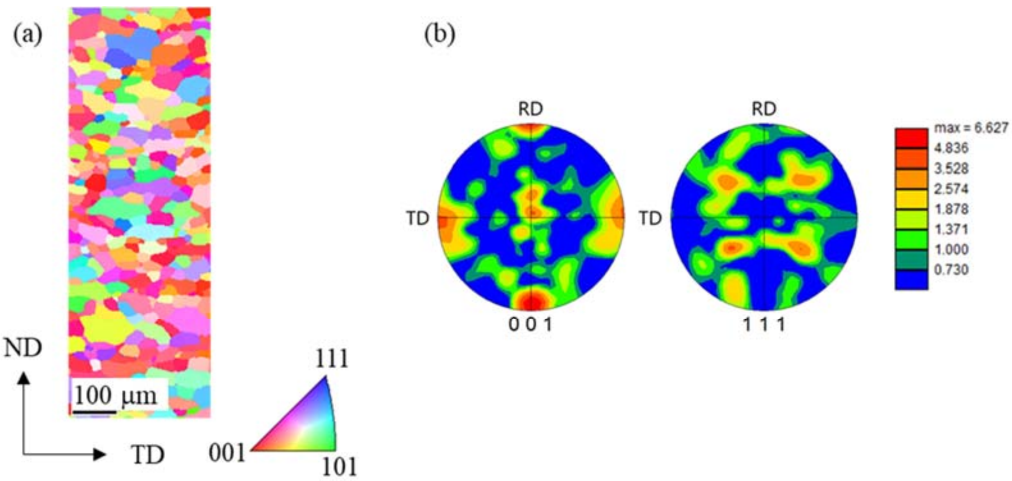

Fig. 1. Microstructures of A6022-T4 sheet used in this study: (a) inverse pole figure map and (b) pole figures

2.2.1 Uniaxial Tensile Tests

To investigate the tensile properties of the material, uniaxial tensile tests were performed along three directions: the rolling direction (RD), transverse direction (TD), and diagonal direction (45D). **Fig. 2** shows the specimen geometry used in this test. The initial strain rate was set to 1.67×10^{-3} s^{-1}. A strain gage (Kyowa Electronic Instrument Co., Ltd., KFEM-5-120-C1L3M3R) was used for the strain measurements. All tests were performed at least twice to confirm reproducibility.

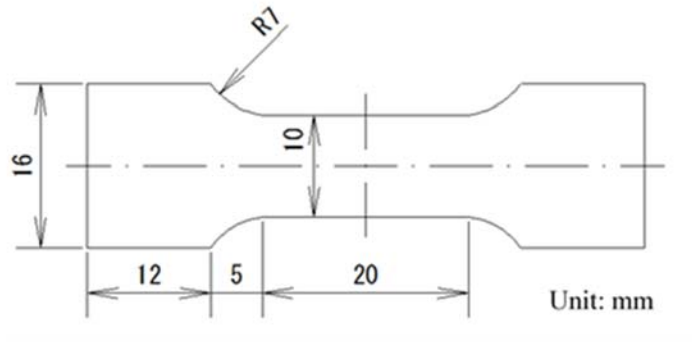

Fig. 2. Geometry of specimen used for uniaxial tensile test

2.2.2 Biaxial Tensile Tests

Biaxial tensile tests were conducted using a cruciform specimen as follows. The specimen geometry is shown in **Fig. 3** (Kuwabara et al., 1998). The arms of the specimen aligned to the RD and TD. All tests were performed at least twice to confirm reproducibility.

The biaxial tensile testing apparatus originally developed by Kuwabara et al. (1998) was used. The biaxial strain components were measured using two strain gauges. The strain gauges were attached 21

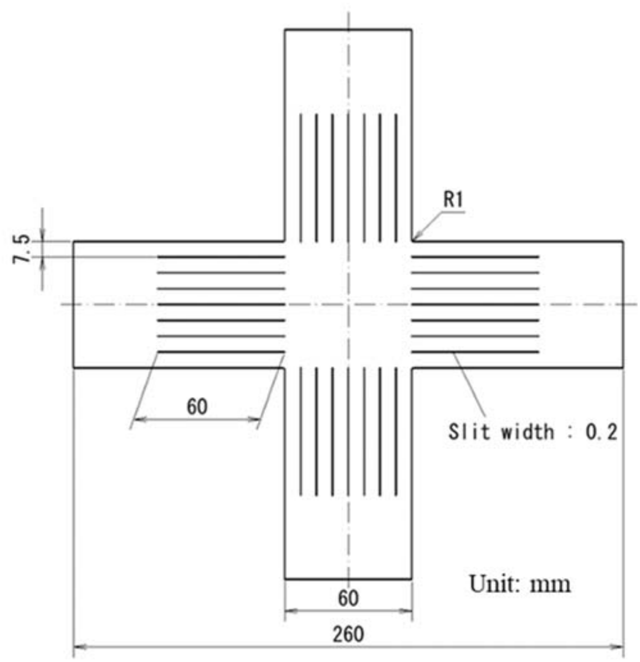

Fig. 3. Geometry of cruciform specimen used for biaxial tensile test (Kuwabara et al., 1998)

mm away from the center of the specimen in the direction of maximum force (Hanabusa et al., 2013). True stress components were calculated using these strain components. The strain gauge used in the biaxial tensile tests was the same as that used in the uniaxial tensile tests.

Force controlled tests were conducted under linear paths to measure the contours of equal plastic work. A schematic illustration of the stress paths is shown in **Fig. 4(a)**. The ratios of true stresses σ_{11} and σ_{22}, which denote the components along the RD and the TD, were controlled to be $\sigma_{11}:\sigma_{22} = 4:1,\ 2:1,\ 4:3,\ 1:1,\ 3:4,\ 1:2$, and $1:4$. The initial strain rate was set to $5.0 \times 10^{-4}\ \mathrm{s}^{-1}$. The results of uniaxial tension along the RD and TD were used for the conditions $\sigma_{11}:\sigma_{22} = 1:0$ and $0:1$, respectively. An anisotropic yield function Yld2000-2d (Barlat et al., 2003) was used to represent the shape of the contour of equal plastic work.

Displacement controlled tests were performed especially focusing on the evolution after abrupt strain-path changes. For comparisons, the conditions of linear strain paths and nonlinear strain paths with gradual change were also conducted. Specifically, the following three different types of loading path were tested to examine the evolution of the plastic flow after strain-path changes.

- Condition 1, shown in **Fig. 4(b)**, was five linear strain paths where the ratios of ε_{11} and ε_{22} were controlled to be $\varepsilon_{11}:\varepsilon_{22} = 1:0,\ 2.414:1,\ 1:1,\ 1:2.414$, and $0:1$. In the following, the angle from the ε_{11} axis in the strain space, which is termed the "strain-path angle," is used to represent the strain path. For instance, the abovementioned linear strain paths correspond to the strain-path angles of $0°,\ 22.5°,\ 45°, 67.5°$, and $90°$, respectively.
- Condition 2, as in **Fig. 4(c)**, was eight nonlinear strain paths involving abrupt change. The sheet was first loaded at $45°$ in the strain space. When the true strains ε_{11} and ε_{22} reached 0.005, the strain path was abruptly altered to $-45°,\ -22.5°,\ 0°,\ 22.5°,\ 67.5°,\ 90°,\ 112.5°$, or $135°$.
- Condition 3, shown in **Fig. 4(d)**, was four nonlinear strain paths involving gradual change. The sheet was first loaded at $45°$ as in the case of condition 2. When the true strains ε_{11} and ε_{22} reached 0.005, the strain path was gradually changed along a circular arc to either $-45°,\ 0°,\ 90°$, or $135°$. The detailed strain paths at the gradual change in the strain paths of $-45°$ and $0°$ are shown in **Fig. 4(e)**. The central coordinate of the circular path was $(\varepsilon_{11}, \varepsilon_{22}) = (0.01, 0)$, and the radius was $0.005\sqrt{2}$.

All the designated loading paths were well reproduced in the experiments, as shown in **Fig. 4**.

Because the purpose of this study was to examine the evolution of plastic deformation behavior after strain-path changes, in the conditions 2 and 3, the maximum force direction along which strain gauges were attached was defined on the basis of the strain path after the path change.

3. Crystal Plasticity Finite-Element Method

3.1. Crystal Plasticity Model

The crystal plasticity model used followed that utilized in previous studies (Hama, et al., 2015, 2017, 2018); thus, it is explained only briefly here. For face-centered cubic (fcc) single crystals, the slip systems are defined by the four $\{111\}$ slip planes and the three $\langle 110 \rangle$ slip directions on each plane. The slip rate of the αth slip system $\dot{\gamma}^{(\alpha)}$ is given by the following equation (Huchinson, 1976;

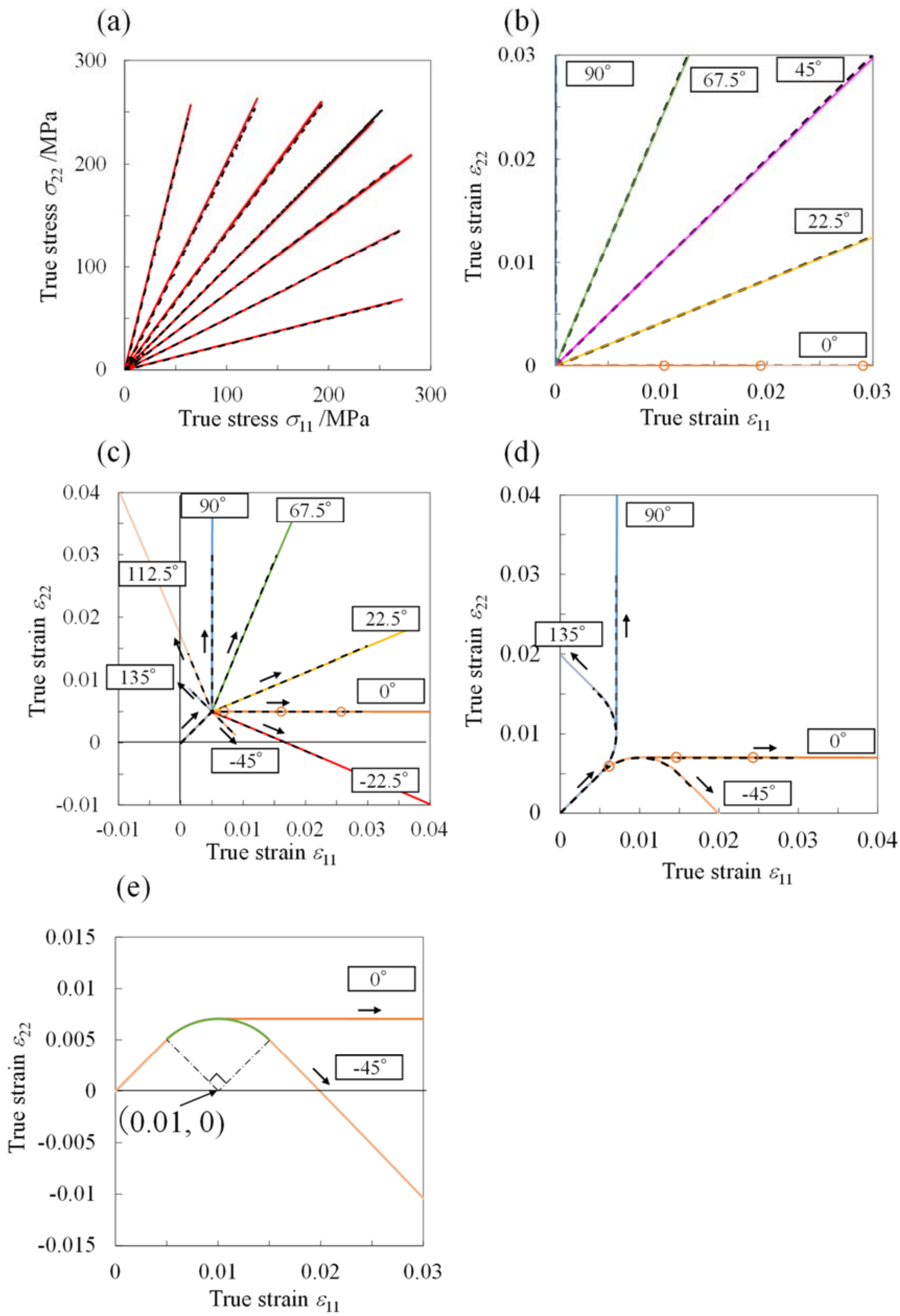

Fig. 4. Loading paths assigned in the experiments and crystal plasticity simulations — solid and broken lines represent the simulation and experimental results, respectively: (a) linear stress paths, (b) linear strain paths (condition 1), (c) nonlinear strain paths with abrupt changes (condition 2), (d) nonlinear strain paths with gradual changes (condition 3), and (e) detailed strain paths in conditions 3, circle marks in (b), (c), and (d) denote the deformation at W_p = 1.3, 3.0 and 5.0 $\mathrm{MJ \cdot m^{-3}}$ for the conditions of 0°

Pierce et al., 1983; Asaro and Needleman, 1985).

$$\dot{\gamma}^{(\alpha)} = \dot{\gamma}_0 \left| \frac{\tau^{(\alpha)}}{\tau_Y^{(\alpha)}} \right|^{\frac{1}{m}} \operatorname{sgn}\left(\tau^{(\alpha)}\right) \quad , \quad \tau^{(\alpha)} = \boldsymbol{s}^{(\alpha)} \cdot \sigma \cdot \boldsymbol{m}^{(\alpha)} \quad , \tag{1}$$

where $\dot{\gamma}_0$ is the reference slip rate, $\tau^{(\alpha)}$ is the resolved shear stress, $\tau_{\mathrm{Y}}^{(\alpha)}$ is the current resistance, and m is the strain rate sensitivity exponent. Here, $\boldsymbol{s}^{(\alpha)}$ and $\boldsymbol{m}^{(\alpha)}$ are the unit vectors that represent the slip direction and the normal to the slip plane, respectively. There are different approaches to utilize Eq. (1) (e.g., Tabourot, 2001; Adzima, et al., 2017). In this work, for convenience, the same parameters were assigned regardless of the slip system, and moreover, $\dot{\gamma}^{(\alpha)}$ was calculated by using Eq. (1) even when $\tau^{(\alpha)}<\tau_Y^{(\alpha)}$. The rate of slip resistance is given by

$$\dot{\tau}_{\mathrm{Y}}^{(\alpha)} = \sum_{\beta} h_{\alpha\beta} \left|\dot{\gamma}^{(\beta)}\right| \quad , \tag{2}$$

where $h_{\alpha\beta}$ is the hardening moduli matrix. On the basis of dislocation-density-based modeling (Teodosiu et al., 1993; Teodosiu, 1997), $h_{\alpha\beta}$ is given in the form

$$h_{\alpha\beta} = \frac{\mu}{2} g_{\alpha\beta} \left(\sum_{\beta} g_{\alpha\beta}\rho^{(\beta)} \right)^{-\frac{1}{2}} \left[\frac{1}{K} \left(\sum_{\beta} d_{\alpha\beta}\rho^{(\beta)} \right)^{\frac{1}{2}} - 2y_c\rho^{(\beta)} \right] \quad , \tag{3}$$

$$\dot{\rho}^{(\alpha)} = \frac{1}{b} \left(\frac{1}{L^{(\alpha)}} - 2y_c\rho^{(\alpha)} \right) \left|\dot{\gamma}^{(\alpha)}\right| \quad , \tag{4}$$

$$L^{(\alpha)} = K \left(\sum_{\beta} d_{\alpha\beta}\rho^{(\beta)} \right)^{-\frac{1}{2}} \quad . \tag{5}$$

where b is the magnitude of the Burgers vector, μ is the shear modulus, and $\rho^{(\alpha)}$ is the dislocation density on the αth slip system. Here, $g_{\alpha\beta}$ is the 12×12 interaction matrix, that models the different types of dislocation interactions, with six independent components. $d_{\alpha\beta}$ is the interaction matrix that defines the interaction between the slip systems (Tabourot, et al., 1997; Fivel, 1998). In addition, y_c and K are material parameters that represent the generation and annihilation processes of dislocations, respectively, and $L^{(\alpha)}$ represents the mean free path of the dislocation of the αth slip system.

3.2. Finite-Element Model

The finite-element model was a cube with length *l*. The cube was uniformly divided into 10 elements in each direction. Eight-node isoparametric solid elements with selective reduced integration were used. The crystallographic orientations were extracted from the result of the EBSD measurements and assigned to Gaussian integration points. A crystallographic orientation was assigned to eight Gaussian integration points in each element. In the simulation, the x-, y-, and z-directions were defined as the RD, TD, and normal direction, respectively. According to the assumption of plane symmetry, the planes $x = 0$, $y = 0$, and $z = 0$ were fixed in the x-, y-, and z-directions, respectively.

The abovementioned finite-element model was used because this model has given sufficiently stabilized macroscopic deformations in our previous studies (Hama and Takuda, 2011, 2012). Moreover, a preliminary study showed that the finite-element model was appropriate also for the present material. Detailed results of the preliminary study are shown in Appendix.

3.3. Simulation Procedures

Displacement increments $\Delta \boldsymbol{u}_x$ and $\Delta \boldsymbol{u}_y$ given, respectively, to the planes $x = l$ and $y = l$ were controlled to simulate the biaxial loadings described in Section 2.2.2. The linear strain paths (condition 1) and nonlinear strain paths with abrupt changes (condition 2) could be achieved by simply adjusting $\Delta \boldsymbol{u}_x$ and $\Delta \boldsymbol{u}_y$ to prescribed strain ratios. The nonlinear strain paths with gradual changes (condition 3) were achieved using the following algorithm. The displacement increments $\Delta \boldsymbol{u}_x$ and $\Delta \boldsymbol{u}_y$ were first imposed while maintaining $|\Delta \boldsymbol{u}_x| = |\Delta \boldsymbol{u}_y|$ until the strains reached 0.005. Then, the ratio of $|\Delta \boldsymbol{u}_x|$ and $|\Delta \boldsymbol{u}_y|$ was controlled to follow a circular arc. For instance, in the cases of $-45°$ and 0°, the circular equation, which is designated by the green solid line in **Fig. 4(e)**, is expressed in the form

$$(\varepsilon_{11} - 0.01)^2 + (\varepsilon_{22})^2 = \left(0.005\sqrt{2}\right)^2 \quad . \tag{6}$$

Solving Eq. (6) with respect to ε_{22} and differentiating with respect to ε_{11} yields

$$\frac{\mathrm{d}\varepsilon_{22}}{\mathrm{d}\varepsilon_{11}} \approx \frac{\Delta \boldsymbol{u}_y}{\Delta \boldsymbol{u}_x} = \frac{1}{2}\left\{(0.005\sqrt{2})^2 - (\varepsilon_{11} - 0.01)^2\right\}^{-1/2} \cdot \left\{-2(\varepsilon_{11} - 0.01)\right\} . \tag{7}$$

To fulfill Eq. (7), $\Delta \boldsymbol{u}_x$ and $\Delta \boldsymbol{u}_y$ were controlled for each step. After the strains reached the prescribed values, the ratio of $|\Delta \boldsymbol{u}_x|$ and $|\Delta \boldsymbol{u}_y|$ was again kept unchanged in accordance with the condition. A similar algorithm was used for the conditions of $135°$ and 90°.

For the stress-controlled paths, an iterative algorithm proposed by Hama and Takuda (2012) was used to achieve pseudo-linear stress paths during deformation.

As shown in **Fig. 4**, all the designated loading paths were well reproduced in the simulations.

3.4. Material Parameters

To represent the elastic anisotropy, the elastic constants were set to $C_{11} = 107$, $C_{12} = 61$, and $C_{44} = 28$ GPa (Simmons and Wang, 1971). The reference slip rate $\dot{\gamma}_0$ in Eq. (1) was set to 0.001 s^{-1}. Following previous studies on Al alloy sheets, the strain rate sensitivity exponent m was set to 0.002 (e.g., Hama et al., 2015). The magnitude of the Burgers vector b was set to 2.86×10^{-10} m. The initial dislocation density $\rho_0^{(\alpha)}$ was assumed to be $1.0 \times 10^{10}\ \mathrm{m}^{-2}$ for all slip systems (Yoshida et al., 2014). The components of the interaction matrixes $d_{\alpha\beta}$ and $g_{\alpha\beta}$ were determined following Madec and Kubin (2017). The parameters τ_0, y_c, and K in Eqs. (3) and (4) were determined so that the predicted uniaxial true-stress–true-strain curve along the RD agreed with the experimental curve. It should be noted that the components of $d_{\alpha\beta}$ and $g_{\alpha\beta}$ were slightly changed from the original values (Madec and Kubin, 2017) to achieve better agreements in the stress-strain curves along the 45D and TD. The values of $d_{\alpha\beta}$, $g_{\alpha\beta}$, τ_0, y_c, and K are listed in **Table 1**.

Table 1. Material parameters for crystal plasticity simulation: g_0, g_1, g_2, g_3, g_4, and g_5, which are the components of $g_{\alpha\beta}$, denote self-hardening, collinear system, Hirth lock, coplanar system, glissile junction, and Lomer–Cottrell sessile lock, respectively

g_0	g_1	g_2	g_3	g_4	g_5	τ_0	y_c	K
0.122	0.810	0.205	0.122	3.20	0.380	54.0	0.65×10^{-5}	20.0

d_0	d_1	d_2	d_3	d_4	d_5
0.122	0.810	1.25	0.122	0.320	0.380

The true-stress–true-strain curves in the RD, TD, and 45D are shown in **Fig. 5(a)**. In the experiment, the flow stress was the largest in the RD, followed in order by the 45D and the TD. This tendency agreed well qualitatively with the results reported for a similar material in a report by Tian et al. (2017). In the simulation, the logarithmic strain tensor was calculated from the averaged deformation gradient by volume averaging of local field of deformation gradient over the reference configuration (Nemat-Nasser, 1999). The simulation results along the RD and the TD agreed well with the experimental results. However, the simulation overestimated the true stresses along the 45D.
Fig. 5(b) shows the evolution of the *r*-value measured by conducting loading–unloading tests for every 1% strain. In the experiment, logarithmic longitudinal and width strains were measured after unloading, and the *r*-value was calculated by $r = \varepsilon_w / (-\varepsilon_w - \varepsilon_l)$, where ε_l and ε_w denote the longitudinal and width strains, respectively.

In the experiment, the *r*-values were almost independent of the tensile strain. The *r*-value was the largest in the RD, followed in order by the TD and 45D. These tendencies, including very-weak *r*-value in the 45D, agreed well with the results reported for similar materials in the literature (Kuwabara, et al., 2017; Tian et al., 2017; Zecevic and Knezevic, 2018; Ogasawara, et al., 2020). These tendencies are typical in Al alloy sheets with strong cube texture. In the simulation results, the magnitude relationship agreed with the experimental results; moreover, the *r*-values were independent of the strain. However, the simulation results along the RD and TD were overestimated.

As shown in Fig. 5, the predictive accuracies of the in-plane anisotropy of the stress-strain curves and the magnitudes of *r*-value were not sufficient and need further improvements. Similar discrepancies were also reported in similar Al alloy sheets in literature (Zecevic and Knezevic, 2018). Advanced crystal plasticity models have been proposed to increase the predictive accuracy (Khadyko, et al., 2016; Zecevic and Knezevic, 2018). Very recently, Feng et al. (2020) predicted successfully the *r*-values by using their crystal plasticity model, although the in-plane anisotropy of the stress-strain curves were still insufficient. In their model, the slip resistance was assumed to consist of the initial resistance and the terms evolving with statistically stored forest and debris dislocations. Further, the total density was assumed to consist of forward and reversible densities of dislocations which were evaluated separately for a positive and negative slip direction. Moreover, the two types of latent hardening matrix as in this study were considered. Although this issue is still open to discussion, such detail treatments of dislocation density would help prediction for 6022-T4 sheets. The improvement of the predictive accuracy will be conducted in our future work.

However, our preliminary studies showed that the effects of parameter identification on the simulation results of strain-path change tests were very small; therefore, the simulation results given in this study are acceptable at least for the purpose of this work.

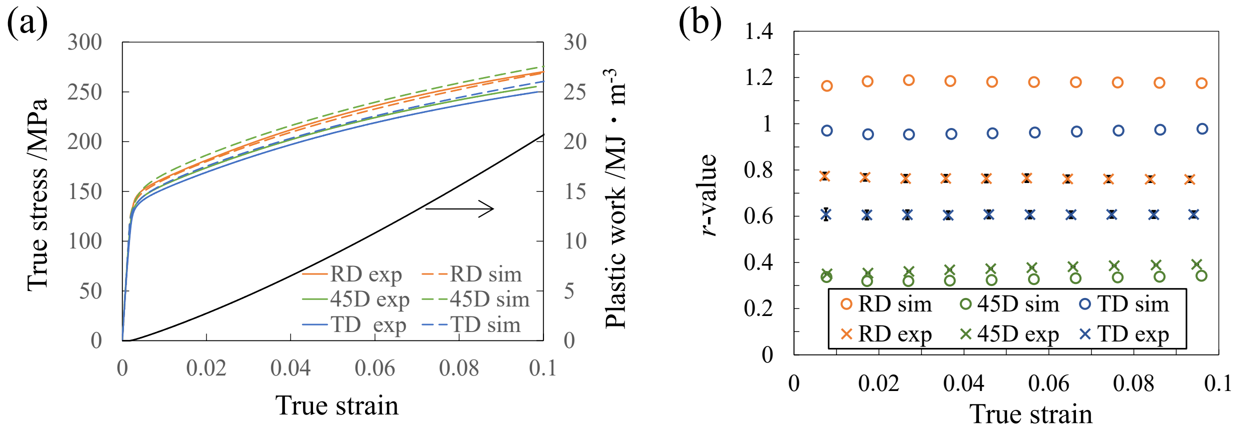

Fig. 5. Uniaxial tensile properties along the RD, 45D, and TD: (a) true-stress–true-strain curves and (b) evolution of the *r*-value — evolution of plastic work during the RD tension is also shown in (a)

4. Experimental and Simulation Results

4.1 Linear Stress Path

Figs. 6(a) and **(b)** show the experimental and simulation results, respectively, of the stress plots of equal plastic work. The stress components $(\sigma_{11}, \sigma_{22})$ were extracted at the plastic works W_p = 0.4, 1.0, 2.0, 4.0, 6.0, and 8.0 $\mathrm{MJ \cdot m^{-3}}$, which corresponded to the strains of approximately 0.005, 0.009, 0.016, 0.027, 0.037, and 0.047 under uniaxial tension in the RD, respectively. Because the plastic work will be used to represent the amount of plastic deformation in the following results, for reference, the relationship between the plastic work and the strain under the RD tension is shown in Fig. 5(a). In the experiment, the results of two specimens were plotted for each stress path. The experimental error was, at most, 4.5 MPa, which was less than approximately 3% of the 0.2% proof stress. The parameters of the Yld2000-2d yield function were determined to describe analytically the shape of the contours of equal plastic work. Given the principal stress state, the Yld2000-2d yield function is given in the form

$$\Phi(\sigma_{11}, \sigma_{22}) = \left|X'_{xx} - X'_{yy}\right|^M + \left|2X''_{yy} + X''_{xx}\right|^M + \left|2X''_{xx} + X''_{yy}\right|^M - 2\bar{\sigma}^M = 0 \quad , \qquad (11)$$

where $\bar{\sigma}$ is the equivalent stress, and

$$\begin{Bmatrix} X'_{xx} \\ X'_{yy} \end{Bmatrix} = \frac{1}{3}\begin{bmatrix} 2\alpha_1 & -\alpha_1 \\ -\alpha_2 & 2\alpha_2 \end{bmatrix}\begin{Bmatrix} \sigma_{11} \\ \sigma_{22} \end{Bmatrix} \quad , \qquad (12)$$

$$\begin{Bmatrix} X''_{xx} \\ X''_{yy} \end{Bmatrix} = \frac{1}{9}\begin{bmatrix} -2\alpha_3 + 2\alpha_4 + 8\alpha_5 - 2\alpha_6 & \alpha_3 - 4\alpha_4 - 4\alpha_5 + 4\alpha_6 \\ 4\alpha_3 - 4\alpha_4 - 4\alpha_5 + \alpha_6 & -2\alpha_3 + 8\alpha_4 + 2\alpha_5 - 2\alpha_6 \end{bmatrix}\begin{Bmatrix} \sigma_{11} \\ \sigma_{22} \end{Bmatrix} \quad . \qquad (13)$$

The results of $\sigma_{11}:\sigma_{22} = 1:0$, $1:1$, and $0:1$ were used to determine α_k (k =1~6). M in Eq. (11) was determined so that the error between the stress points and the Yld2000-2d curve was minimized

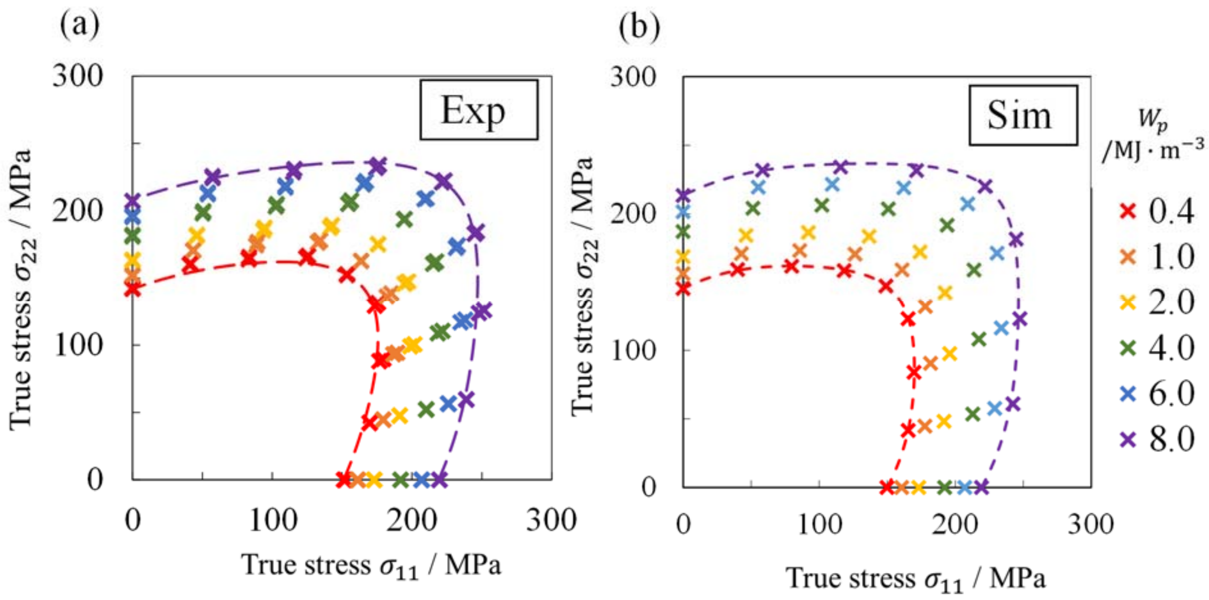

Fig. 6. Contours of equal plastic work with Yld2000-2d yield loci (broken lines): (a) experimental and (b) crystal plasticity simulation results

(Kuwabara and Yoshida, 2015). Here, α_k (k =1~6) and M were determined at the plastic works of 0.4 and 8.0 $\mathrm{MJ \cdot m^{-3}}$. The determined values are listed in **Table 2**. Because the stress plots were different between the experimental and simulation results, the parameters were determined separately for the experimental and simulation results to achieve the best fit for each result.

The determined Yld2000-2d yield loci are shown in **Fig. 6**. In the experiment, small differences appeared between the stress plots and the yield locus at $\sigma_{11}:\sigma_{22} = 1:4$ for W_p = 0.4 $\mathrm{MJ \cdot m^{-3}}$, whereas the yield locus described the stress plots well for W_p = 8.0 $\mathrm{MJ \cdot m^{-3}}$. In the simulation, the yield loci described the stress plots well for both plastic works. The predicted yield loci were apparently different from those of the experimental ones, as explained earlier.

Fig. 7 shows the relationships between the stress ratio φ and the direction of the plastic strain rate θ for W_p = 0.4 and 8.0 $\mathrm{MJ \cdot m^{-3}}$, which are defined as follows:

$$\varphi = \arctan \frac{\sigma_{22}}{\sigma_{11}} \quad , \tag{14}$$

$$\theta = \arctan \frac{d\varepsilon_{22}^{p}}{d\varepsilon_{11}^{p}} \quad . \tag{15}$$

The reference results calculated using the associated flow rule with the Yld2000-2d yield function are also shown. The differences in θ between the reference and experimental results were, at most, approximately 8.7° and 5.5°, respectively, for W_p = 0.4 and 8.0 $\mathrm{MJ \cdot m^{-3}}$. These results indicate that the deformation behavior under the linear stress paths was reproduceable using the associated flow rule within these errors. Because the difference in the reference results between W_p = 0.4 and 8.0 $\mathrm{MJ \cdot m^{-3}}$ was also within comparable small errors, it is reasonable to assume that this material exhibits isotropic hardening. Similarly, in the simulation results in **Fig. 7(b)**, the plastic flow was also well represented by the associated flow rule for both plastic works, which is consistent with the

Table 2. Parameters of Yld2000-2d yield function determined for experimental and crystal plasticity simulation results

	W_p / $\mathrm{MJ \cdot m^{-3}}$	M	α_1	α_2	α_3	α_4	α_5	α_6
exp	0.4	4.6	0.693	1.187	1.011	1.077	0.994	0.697
	8.0	5.6	0.941	0.982	0.892	1.058	1.002	0.899
sim	0.4	6.0	0.967	1.073	1.069	1.034	0.984	0.941
	8.0	7.0	0.985	1.046	0.999	1.022	0.981	0.940

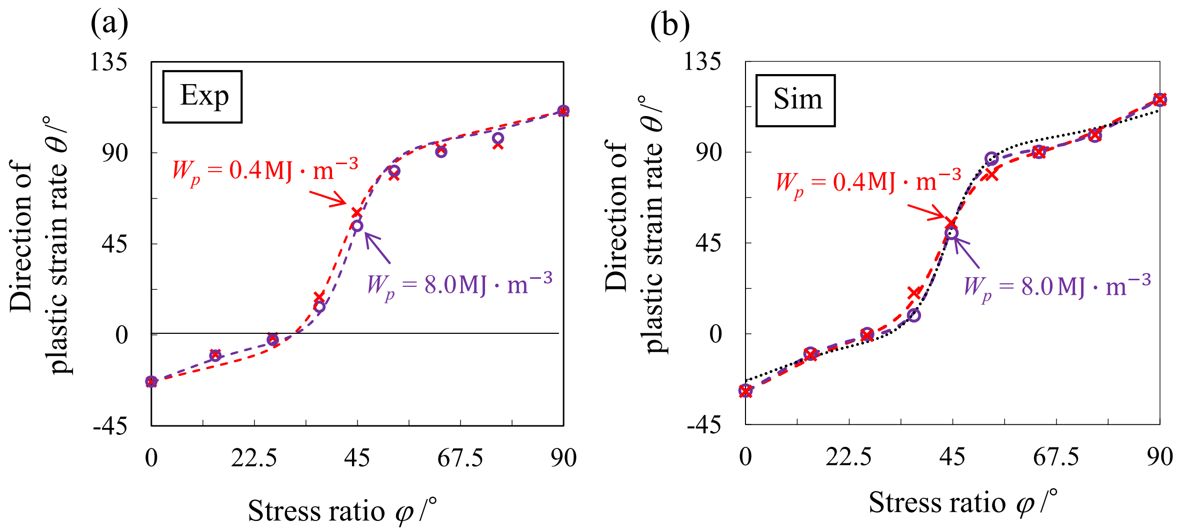

Fig. 7. Relationships between φ and θ under linear stress paths obtained from (a) experiment and (b) crystal plasticity simulation: dots are obtained from biaxial tensile tests, and broken lines are the reference results calculated using the associated flow rule with the Yld2000-2d yield function. In (b) dotted line is the reference results of the experimental result for $W_p = 8.0$ MJ $\cdot$ m^{-3}

experimental results.

As described earlier, the yield loci were different between the experimental and simulation results. To examine the difference more in detail, the reference result of the experiment for $W_p = 8.0$ MJ $\cdot$ m^{-3} is also shown in Fig. 7 (b). The difference in θ between the two reference results was at most 5.3°. It is presumed that this level of error is involved when the experimental and simulation results are directly compared. For this reason, to eliminate the effect of the difference in the reference results from discussion, the results of the associated flow rule with the Yld2000-2d yield function at $W_p = 8.0$ MJ $\cdot$ m^{-3} and isotropic hardening assumption obtained for the experimental and simulation results were used as the reference results for the experiment and simulation, respectively.

It is noted that currently there is no evidence that the abovementioned isotropic hardening assumption holds after strain-path changes. Therefore, the evaluation of the normality after strain-path changes was not discussed in this study. However, because the associated flow rule is still often used in industrial FEM simulations, as explained earlier, it is worth comparing experimental and simulation results with the reference results to examine the representability of the plastic deformation after strain-path changes by using the associated flow rule, an initial yield surface, and the isotropic hardening assumption from practical viewpoints. In addition, another reason to compare with the reference results was that it is helpful to use reference results to discuss comprehensively the plastic deformation behaviors under different loading paths.

On the basis of the past studies, it is presumed that the plastic deformation for conditions 1 and 3 is representable by the reference results throughout the process because any bifurcation is not involved, whereas that of condition 2 deviates from the reference results just after the strain path changes.

4.2 Linear Strain Path

Figs. 8(a) and **(b)** show, respectively, the transitions of θ as a function of plastic work and the stress evolution under the linear strain paths (condition 1). For the experimental results shown in Fig. 8 (a), the results from W_p = 0.4 $\mathrm{MJ \cdot m^{-3}}$ until fracture are shown. The experiments could be conducted to the plastic work range from approximately 5.0 to 9.0 $\mathrm{MJ \cdot m^{-3}}$. In the experimental and simulation results, the changes in θ were very small except for the very beginning of deformation.

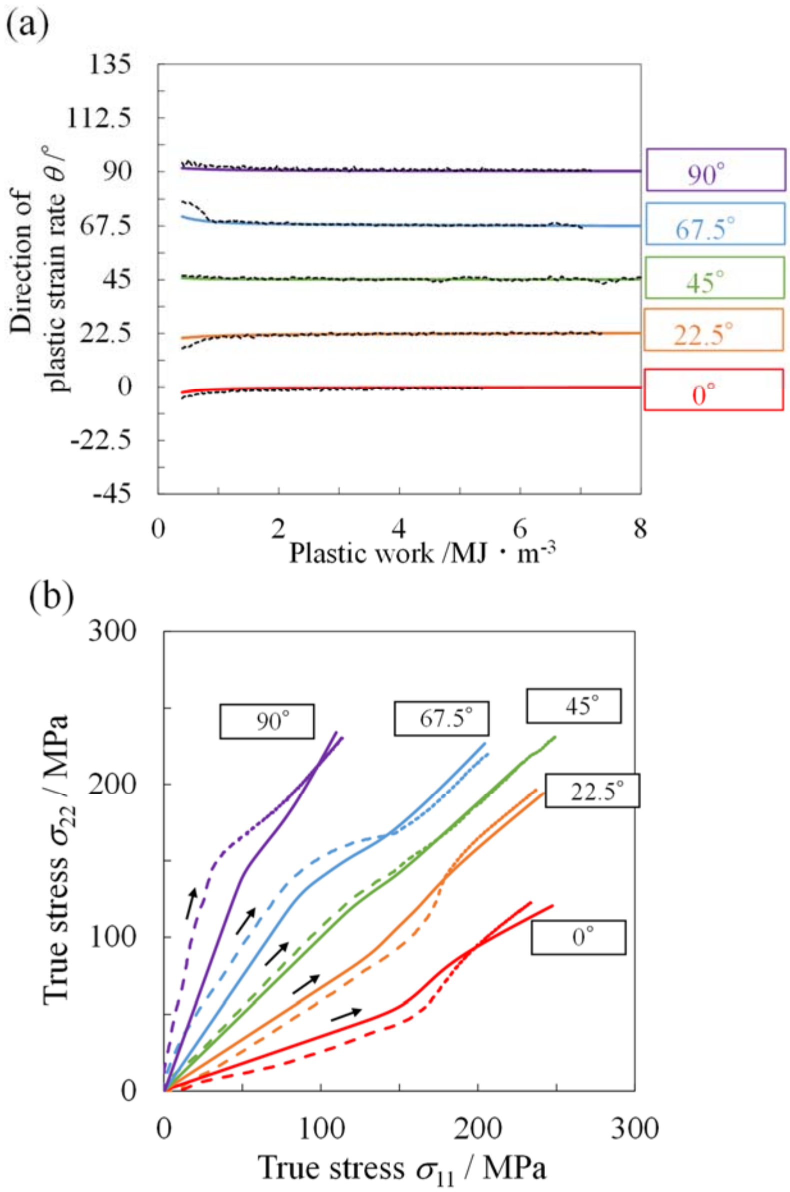

Fig. 8. Results of linear strain paths (condition 1): (a) transitions of θ as a function of plastic work and (b) evolution of stresses — the broken and solid lines denote the experimental and crystal plasticity simulation results, respectively

This tendency was also independent of the strain path. The values of θ matched well the strain-path angles for all conditions. The stress evolution was nonlinear, irrespective of the path. The nonlinear evolution would be owing to the anisotropy of the material (Kuwabara, et al., 2000). The simulation results reproduced the overall tendencies observed in the experimental results of the transition of θ. In the stress evolution, although overall tendencies were reproduced well, quantitative differences were somewhat large for stresses under 200 MPa. The reason of this difference will be discussed in Section 4.5.

Fig. 9 (a) shows the experimental results of the relationships between φ and θ during deformation for condition 1. For the condition of 45°, the values of φ and θ remained almost unchanged throughout the process and were almost on the reference curve. In contrast, for the conditions of 0°, 22.5°, 67.5°, and 90°, the relationships evolved in the directions designated by the arrows because the stress ratio apparently changed, see Fig. 8 (b). The trajectories roughly followed the reference curve, although they were not exactly on it. Specifically, the differences in θ between the reference and experimental results during deformation were, at most, approximately 7.0°, which was comparable to those observed in Fig. 7. After the relationships reached the × marks at W_p = 5.0 $\mathrm{MJ \cdot m^{-3}}$, which corresponded to the strain of approximately 0.032 under uniaxial tension in the RD, further deformation until fracture was very small. For the condition of 0°, the change in θ was approximately 4.3° from W_p = 0.4 to 5.0 $\mathrm{MJ \cdot m^{-3}}$, while it was approximately 0.3° from W_p = 5.0 $\mathrm{MJ \cdot m^{-3}}$ to fracture at W_p = approximately 5.4 $\mathrm{MJ \cdot m^{-3}}$. These results suggested that the plastic deformation behavior under linear strain paths could be evaluated by using the associated flow rule with the Yld2000-2d yield function and isotropic hardening assumption with practical small errors, irrespective of the strain path.

Fig. 9 (b) shows the simulation results. The results in the plastic work range from 0.4 to 8.0 $\mathrm{MJ \cdot m^{-3}}$ are shown. The trajectories were almost on the reference curve, and the results were qualitatively the same with those of the experiments. In all the conditions, the values of φ and θ remained almost unchanged beyond W_p = 5.0 $\mathrm{MJ \cdot m^{-3}}$. More specifically, for the condition of 0°, the change in θ was approximately 2.0° from W_p = 0.4 to 5.0 $\mathrm{MJ \cdot m^{-3}}$, while it was less than 0.1° from W_p = 5.0 to 8.0 $\mathrm{MJ \cdot m^{-3}}$. These experimental and simulation results suggest that the deformation roughly converged at W_p = around 5.0 $\mathrm{MJ \cdot m^{-3}}$.

4.3 Nonlinear Strain Path with Abrupt Change

Figs. 10(a) and **(b)** show, respectively, the transitions of θ as a function of plastic work and the stress evolution under the nonlinear strain paths with abrupt change (condition 2). In the experimental and simulation results, θ was 45° before the path changes, as shown in **Fig. 10(a)**. This is consistent with the result of the linear strain path (**Fig. 8**). After the strain paths abruptly changed at W_p = approximately 1.0 $\mathrm{MJ \cdot m^{-3}}$, θ rapidly changed to the angles designated by each strain path and then tended to converge. For the conditions of –45°, 112.5° and 135°, the experiments could not be conducted until convergence because the sign of either σ_{11} or σ_{22} became negative before

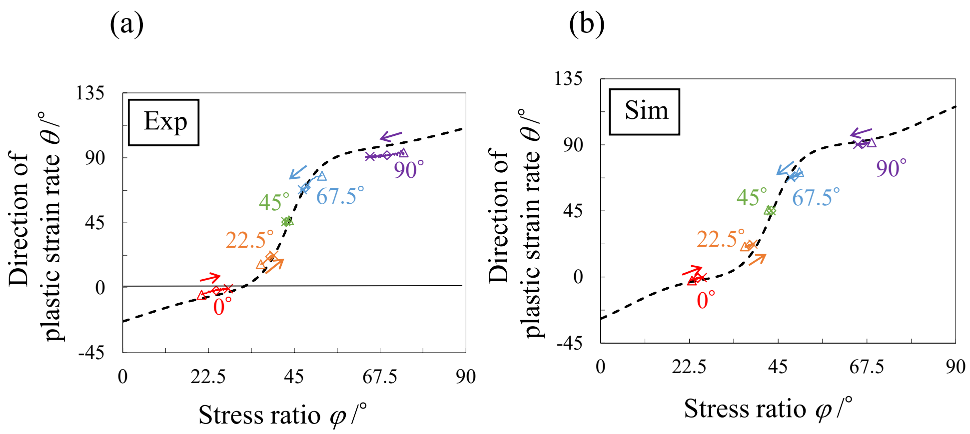

Fig. 9. Relationships between φ and θ for linear strain paths (condition 1) obtained from (a) experiment and (b) crystal plasticity simulation: the broken lines are the reference curves, and △, ◇, and X denote the deformation at $W_p = 0.4$, 1.3 and 5.0 $\mathrm{MJ \cdot m^{-3}}$, respectively

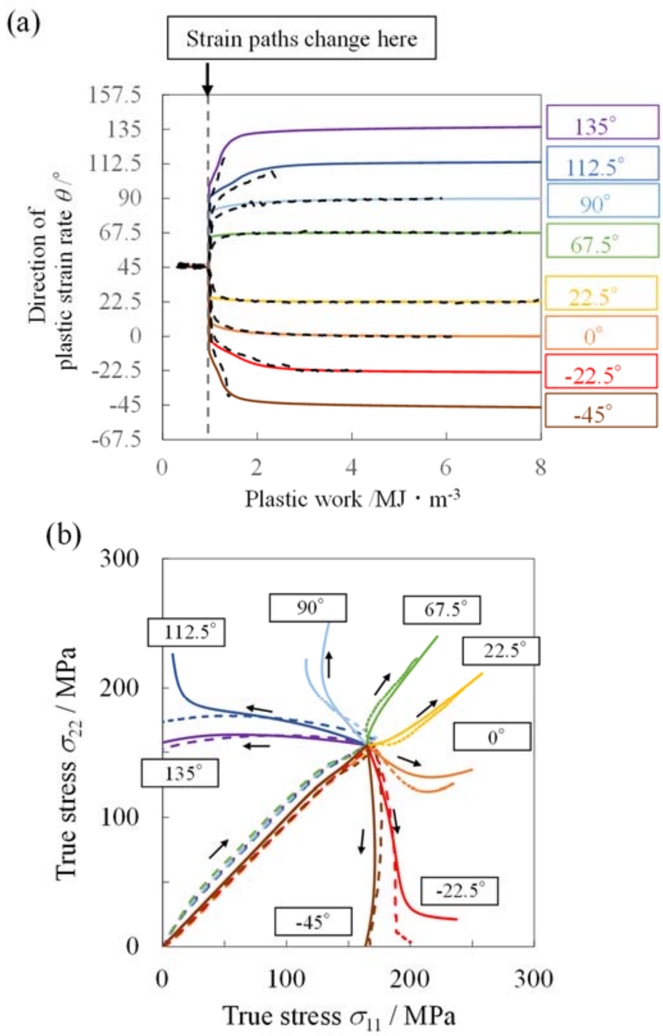

Fig. 10. Results of nonlinear strain paths with abrupt changes (condition 2): (a) transitions of θ as a function of plastic work and (b) evolution of stresses — the broken and solid lines denote the experimental and crystal plasticity simulation results, respectively

convergence. In other words, it is presumed that θ tends to converge also for these conditions if the experiments can be conducted to the second or fourth quadrants in the stress space.

As discussed in previous studies (Hill et al., 1994; Kuroda and Tvergaard, 1999; Kuwabara et al., 2000), the stress paths for the strain-path angles of −45° and 135° corresponded to a subsequent yield surface, which lay within the contour of plastic work shown in **Fig. 6 (b)**. Clear vertices appeared at the strain-path change points, consistent with the work by Kuwabara et al. (2000). The simulation results reproduced the overall tendencies observed in the experimental results of the transitions of θ and the stress evolution.

Fig. 11 shows the relationships between φ and θ for condition 2. For comparison, the results of condition 1 are also shown for the conditions of 0°, 22.5°, 67.5°, and 90°. In the experimental results in **Fig. 11(a)**, before the strain paths changed, the relationships were within the black circle, irrespective of the strain path, and were almost on the reference curve. Immediately after the strain paths changed, the relationships rapidly deviated from the reference curve to the directions designated by the arrows — that is, the slopes of the trajectories were significantly different from that of the reference curve. More specifically, for the condition of 0°, the difference in θ between the experimental and reference curves just after the paths changed was at most 11°. The slopes of the trajectories were almost independent of the strain path. Thereafter, the slopes rapidly changed, and the relationships approached to the reference curve. The smaller the change in the strain-path angle, the earlier the slope changed. After the relationships reached the × marks at W_p = 5.0 $\mathrm{MJ \cdot m^{-3}}$, they remained almost unchanged until fracture as in the case of condition 1, suggesting that the deformation roughly converged at the × marks. More specifically, for the condition of 0°, the change in θ was approximately 7.4° from W_p = 1.3 to 5.0 $\mathrm{MJ \cdot m^{-3}}$, while it was less than 0.1° from W_p = 5.0 $\mathrm{MJ \cdot m^{-3}}$ to fracture at W_p = approximately 6.1 $\mathrm{MJ \cdot m^{-3}}$. Because the × marks were very close to those of condition 1, it can be said that the plastic deformation behavior at the plastic work larger than 5.0 $\mathrm{MJ \cdot m^{-3}}$ could eventually be represented by using the reference curve within practical small errors. This result also suggests that the plastic work increment of roughly 4.0 $\mathrm{MJ \cdot m^{-3}}$, which corresponded to the strain increment of approximately 0.024 under uniaxial tension in the RD, was necessary until the deformation could be represented again by the reference curve after abrupt changes.

The simulation results in **Fig. 11(b)** showed similar overall tendencies, but the deviation from the reference curve just after the path change was overestimated. More specifically, for the condition of 0°, the difference in θ between the simulation and reference curves just after the paths changed was at most 31°. The values of φ and θ remained almost unchanged beyond W_p = 5.0 $\mathrm{MJ \cdot m^{-3}}$. For the condition of 0°, θ changed approximately 4.8° from W_p = 1.3 to 5.0 $\mathrm{MJ \cdot m^{-3}}$, while it changed approximately 0.27° from W_p = 5.0 to 8.0 $\mathrm{MJ \cdot m^{-3}}$. The × marks were close to those of condition 1, as in the case of the experiment, but the deviation of the × marks between conditions 1 and 2 was larger than that of the experimental results.

Yang and Balan (2019) have also conducted simulations with the condition of -45° using a phenomenological elasto-viscoplastic model, and the relationship between the direction of viscoplastic

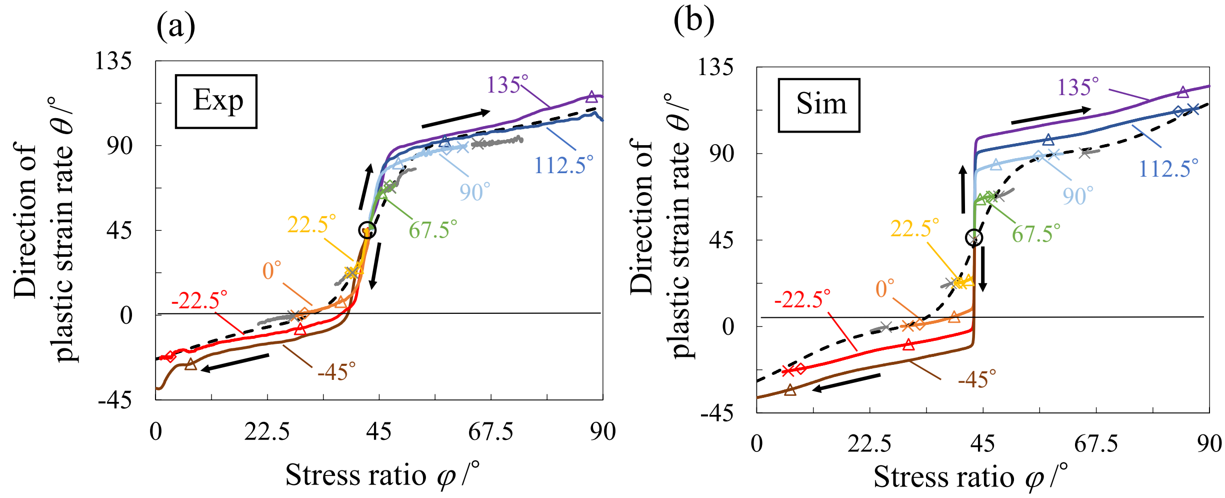

Fig. 11. Relationships between φ and θ for nonlinear strain paths with abrupt changes (condition 2) obtained from (a) experiment and (b) crystal plasticity simulation: the broken lines show the reference curves, solid gray lines show the results of condition 1, and △, ◇, and X denote the deformation at W_p = 1.3, 3.0 and 5.0 $\mathrm{MJ \cdot m^{-3}}$, respectively

strain rate and the stress ratio has been studied. The abovementioned tendencies, i.e., the slope just after the path change was significant and then it rapidly decreased and the relationships approached to the reference curve, were consistent with their work.

4.4 Nonlinear Strain Path with Gradual Change

Figs. 12(a) and **(b),** respectively, show the transitions of θ as a function of plastic work and the stress evolution under the nonlinear strain paths with gradual change (condition 3). In the experimental and simulation results, the tendencies of the transitions of θ were similar to those under abrupt changes, although the slopes just after the path change were smaller. The stress evolution was also similar to that shown in **Fig. 10(b)**, but a vertex did not appear when the strain path changed. The simulation results reproduced the overall tendencies observed in the experimental results of the transitions of θ and the stress evolution. For the conditions of –45° and 135°, the experiments could not be conducted until convergence because the sign of either σ_{11} or σ_{22} became negative before convergence.

Fig. 13 shows the relationships between φ and θ for condition 3. For comparison, the results of condition 1 are also shown for the conditions of 0° and 90°. In the experimental results, the relationships were within the black circle before the path change, as in the case of condition 2. After the paths changed, the trajectories tended to follow the reference curve. In the case of the conditions of 0° and 90°, the circular strain paths finished at W_p = approximately 2.2 $\mathrm{MJ \cdot m^{-3}}$, and the strain paths became linear, as shown in Fig. 4 (d). After the relationships reached the × marks at W_p = 5.0 $\mathrm{MJ \cdot m^{-3}}$, they remained almost unchanged until fracture. The × marks were very close to those of condition 1, consistent with condition 2.

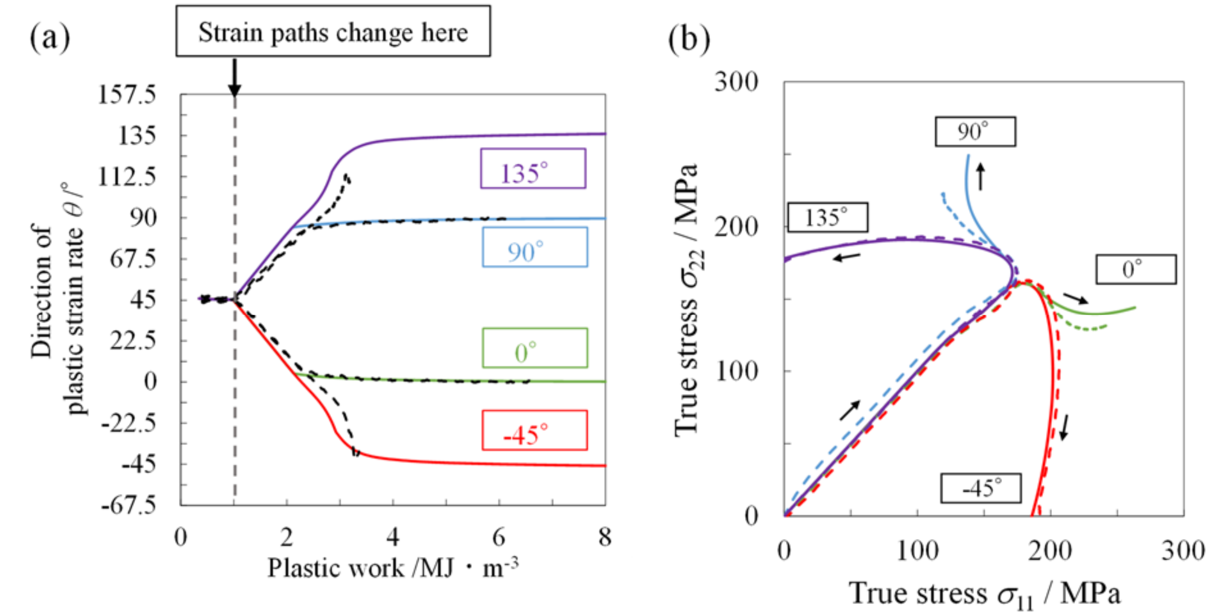

Fig. 12. Results of nonlinear strain paths with gradual changes (conditions 3 and 4): transitions of θ as a function of plastic work for (a) condition 3 and (b) condition 4, and evolution of stresses for (c) condition 3 and (d) condition 4 — the broken and solid lines denote the experimental and crystal plasticity simulation results, respectively

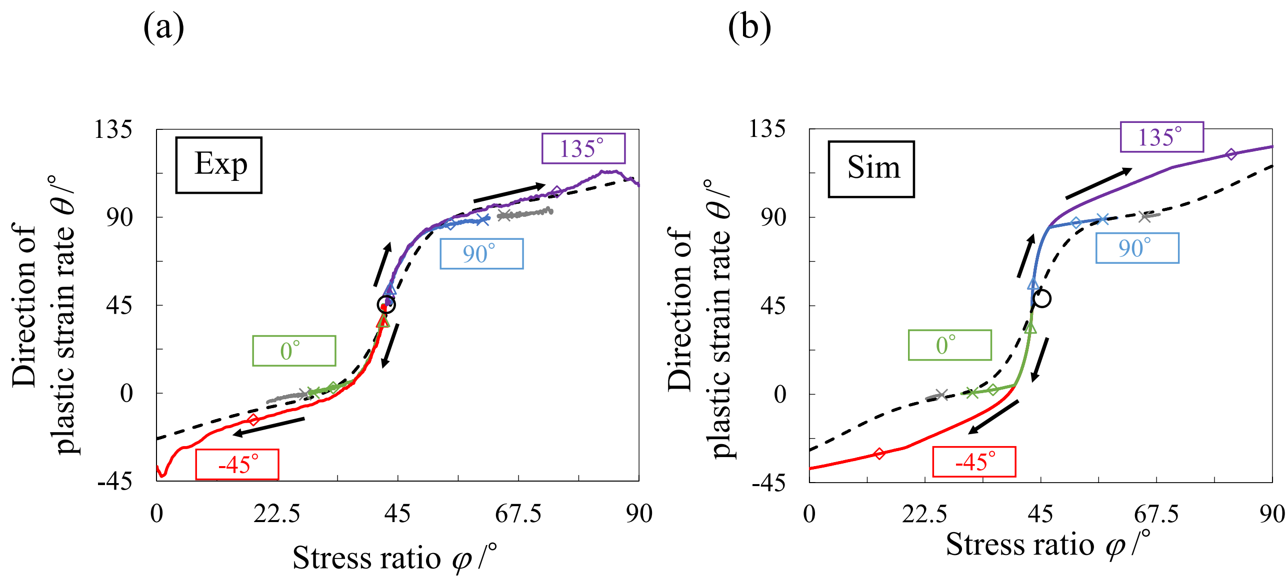

Fig. 13. Relationships between φ and θ for nonlinear strain paths with gradual changes (conditions 3 and 4) obtained from (a) experiment and (b) crystal plasticity simulation: the broken lines show the reference curve, solid gray lines show the results of condition 1, and △, ◇, and X denote the deformation at W_p = 1.3, 3.0 and 5.0 MJ $\cdot$ m^{-3}, respectively

However, in the simulation results, the slopes of the trajectories immediately after the path change were still largely different from the reference curve, followed by approaching to the reference curve. More specifically, for the condition of 0°, the difference in θ between the simulation and reference curves during this process was at most 19°. However, it is also apparent that the deviation from the reference curve was less pronounced than that of condition 2, which is qualitatively consistent with the experimental results. As in the cases of condition 2, the values of φ and θ remained almost unchanged beyond W_p = 5.0 $\mathrm{MJ \cdot m^{-3}}$, and the $\times$ marks were close to those of condition 1.

4. 5 Summary of Results

In the present study, the evolution and convergence of plastic deformation after strain-path changes could be successfully measured in the experiments. The trajectories on the $\varphi-\theta$ plane roughly followed the reference curve under conditions 1 and 3 within practical small errors, as expected from the past studies. These results suggest that the plastic deformation behavior of the present material can be practically represented by using the associated flow rule with the Yld2000-2d yield function and isotropic hardening assumption when the strain-path change is gradual or not involved. It should be noted that the agreement between the experimental and reference curves did not mean that the normality was fulfilled theoretically, because there is no evidence that the isotropic hardening assumption is valid also after strain-path changes, as explained earlier. On the other hand, when the strain-path change was abrupt (condition 2), the trajectories were far different from the reference curve just after path changes, while they then could be represented again by using the reference curve within practical small errors at the plastic work larger than 5.0 $\mathrm{MJ \cdot m^{-3}}$. These results were qualitatively consistent with the literature (Kuroda and Tvergaard, 1999; Kuwabara et al., 2000; Yang and Balan, 2019).

The simulation reproduced the qualitative tendencies observed in the experiments, but in the strain-path change conditions (conditions 2 and 3), the deviations from the reference curve just after the paths changed were much more pronounced than in the experimental results.

The experimental and simulation results suggested that the deformation roughly converged at W_p = around 5.0 $\mathrm{MJ \cdot m^{-3}}$ after the strain path changed at W_p = approximately 1.0 $\mathrm{MJ \cdot m^{-3}}$. Moreover, if the strain-path angle after the path change was the same, the converged points were very close irrespective of the condition.

Lastly, the difference in the stress evolution between the experiments and simulations are briefly discussed. In the stress evolution in condition 2 (Fig. 10 (b)), the stress evolution before path change was apparently different between the conditions of the strain-path angles $\leq$ 22.5° and $\geq$ 67.5°. Specifically, the differences in the stress states between the two conditions were estimated to be at most 15 % and 3 % before and at the strain-path change point, respectively. This difference occurred presumably because the measurements of strains, i.e., the positions where strain gauges were attached, were different. Similar levels of errors would be involved also in conditions 1 and 3. On the other hand, the elastic constants used in the simulation could also yield the deviation in the stress evolution before the path changes between the experiment and the simulation. The elastic constants used in this study were taken from a literature (Simmons and Wang, 1971) as explained earlier, but there is no evidence that these parameters are acceptable for the present material. Therefore, it is considered that both experimental and predictive accuracies should be improved to obtain better agreements in the stress evolution.

5. Discussion

5.1. Effect of Strain Path

5.1.1 Experimental Results

The results of condition 2, where large deviation from the reference curve appeared, are discussed in detail. To this end, the results of conditions 1, 2, and 3 with a strain-path angle of 0° are used to discuss the effect of the strain path on the plastic deformation behavior after the path changes.

Figs. 14 (a) and (b) show the experimental results of the transitions of θ and φ as a function of plastic work for the three strain paths, respectively. In Fig. 14 (b), reference transitions of φ calculated using the transitions of θ and the associated flow rule with the Yld2000-2d yield function are also shown. After the paths changed at the plastic work of approximately 1.0 $\mathrm{MJ \cdot m^{-3}}$, θ and φ tended to converge to approximately 0° and 28° regardless of the strain path, suggesting that both θ and φ tended to converge to certain values whether or not deviation from the reference curve appeared after strain path changes. These results are consistent with Figs. 9, 11, and 13. In the present case, θ and φ almost converged at plastic works of around 5.0 $\mathrm{MJ \cdot m^{-3}}$, suggesting that the plastic work increment of approximately 4.0 $\mathrm{MJ \cdot m^{-3}}$, which corresponded to the strain increment of approximately 0.024 under RD tension, was necessary after strain-path change before the plastic deformation converged, as also explained earlier. It should be noted that for conditions 1 and 3 the experimental curves were in good agreements with the reference curves throughout the process even though the deformation did not converge at plastic works smaller than 5.0 $\mathrm{MJ \cdot m^{-3}}$.

The transitions of θ and φ are discussed in detail for each condition. In condition 1, both θ and φ varied extremely gradually throughout the process. Comparing the transition of φ with the reference curve, the experimental result was 2° to 4° smaller than the reference curve. Moreover, the experimental result of the final angle of φ was slightly smaller than that of the reference curve. This quantitative difference was comparable to that observed in **Figs. 7** and **9**. However, the transition tendencies were similar, and the experimental result qualitatively followed the reference curve, which is consistent with **Fig. 9**.

In contrast, for conditions 2 and 3, the changes in both θ and φ immediately after the path changes were sharp. To examine the evolution of φ in detail, **Fig. 14 (c)** shows the transitions of instantaneous gradient of φ. For visibility purposes, only the results of conditions 2 and 3 are shown.

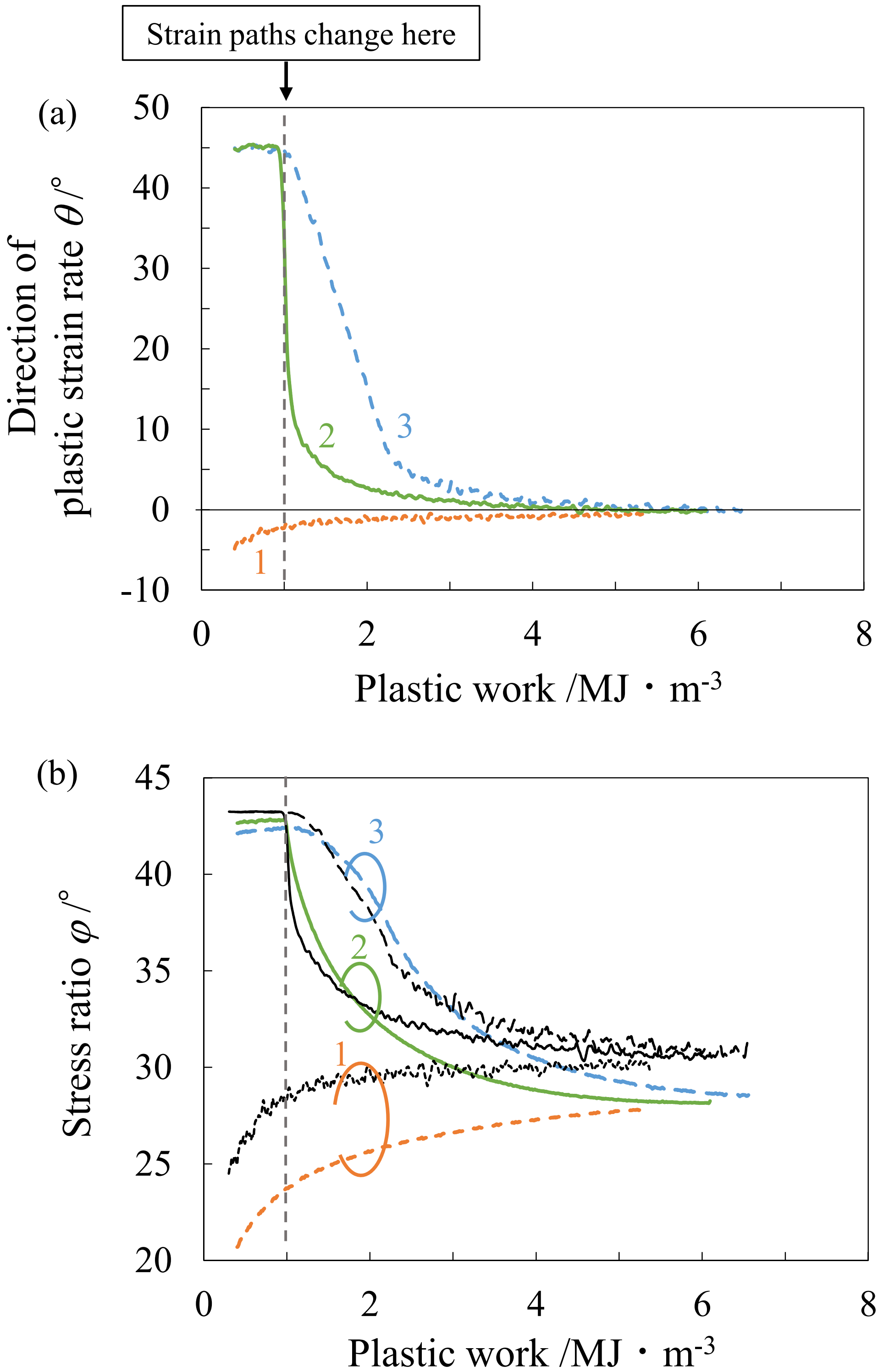
Strain paths change here
(a)
Direction of plastic strain rate θ/°
50
40
30
20
10
0
-10
0
2
4
6
8
Plastic work /MJ・m-3
1
2
3
(b)
Stress ratio φ/°
45
40
35
30
25
20
0
2
4
6
8
Plastic work /MJ・m-3
1
2
3

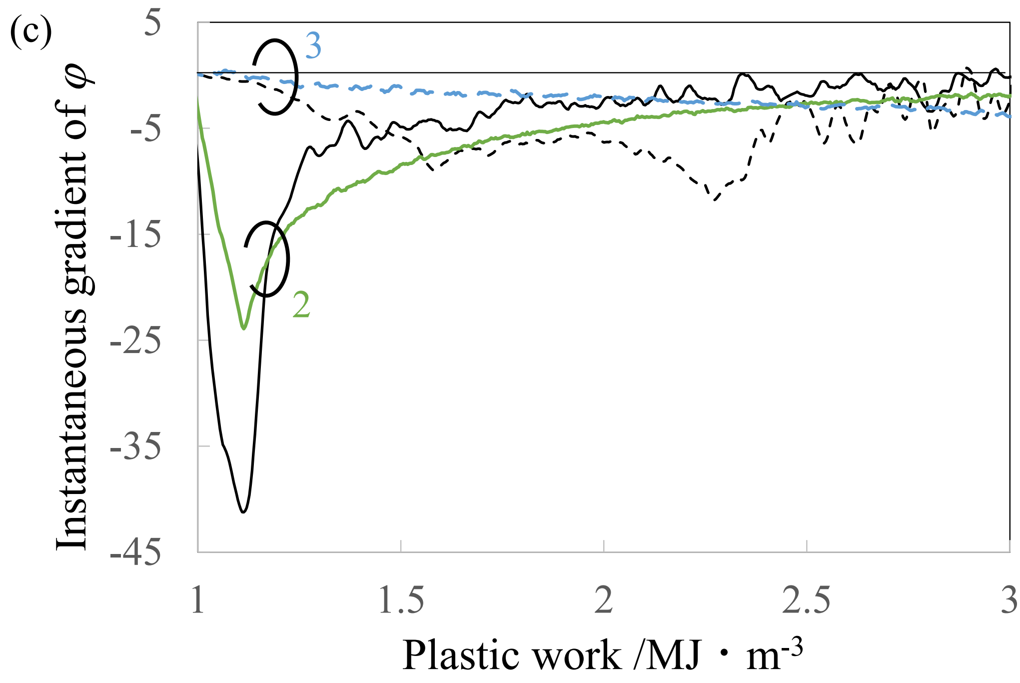

Fig. 14. Experimental results of transitions of θ and φ as a function of plastic work for conditions 1, 2, and 3 with a strain-path angle of 0° : (a) Transitions of θ, (b) transitions of φ, and (c) transitions of instantaneous gradient of φ — In (b) and (c), the black lines are the reference results, and the numbers given to the curves denote conditions

In condition 3, the gradient gradually decreased. Because the trajectory in the θ - φ plane was represented by the reference curve with practical small errors for condition 3 (Fig. 13), the deviation in the gradient observed in Fig. 14 (c) can also be considered as acceptable errors.

In condition 2, the change in θ immediately after the path change, i.e., specifically in the plastic work range from 1.0 to 1.2 $\mathrm{MJ\cdot m^{-3}}$, was much more pronounced than in the other conditions (Fig. 14 (a)). However, the gradient of φ in this range was apparently smaller in the experimental result than in the reference curve. These results indicate that the relationships between φ and θ temporarily deviated from the reference result immediately after the path changes in condition 2 (**Fig. 11**) because the transition of φ was too gradual compared with the reference curve — that is, φ could not follow the rapid change of θ immediately after the abrupt change. Moreover, it is also presumed that the deviation from the reference curve was governed primarily by the deformation in the plastic work range from 1.0 to 1.2 $\mathrm{MJ\cdot m^{-3}}$, which corresponded to a strain increment of approximately 0.001 under uniaxial tension in the RD.

Because the shape of yield locus would be subjected to change when the strain paths changed, as described earlier, it is significant to take this effect into consideration when the applicability of the associated flow rule is discussed more rigorously. For instance, considering the homogeneous anisotropic hardening approach (Barlat, et al., 2011; 2013), it is presumed that the shape of yield locus is subjected to notable change after an abrupt path change, in particular for the plastic deformation from the plastic work of 1.0 to 5.0 MJ/m^{-3} in Fig. 14. It is expected that the change in the shape of the yield locus under the associated flow rule can be discussed in detail by utilizing the present experimental results and the homogeneous anisotropic hardening approach, which will be a part of our future works.

5.1.2 Simulation Results

Fig. 15 shows the simulation results of the transitions of θ and φ for the three strain paths discussed in Section 5.1.1. The experimental results are also shown. The deviations in θ between the simulation and experimental results slightly appeared until W_p = 3.0 $\mathrm{MJ \cdot m^{-3}}$. They then almost disappeared at W_p = 5.0 $\mathrm{MJ \cdot m^{-3}}$, and θ converged to 0° irrespective of the condition. In contrast, the changes in φ were more gradual in the simulation results than in the experimental results irrespective of the condition. Moreover, although the subsequent changing rates were very small, φ still depended on the condition even at W_p = 5.0 $\mathrm{MJ \cdot m^{-3}}$. These results suggest that the present simulation tended to yield a more gradual transition of φ than the experimental results, which eventually yielded larger deviations of the relationship between φ and θ from the reference results of the associated flow rule in conditions 2 and 3. Furthermore, it is also presumed that the convergence points in the θ - φ plane were different between the experimental and simulation results primarily because of the deviation in φ.

Because θ would primarily be governed by slip activities, the correlation with the activities of slip systems was examined. The activities of the 12 slip systems of the fcc structure were evaluated using the relative activity of the αth slip system $r^{(\alpha)}$ as follows.

$$r^{(\alpha)} = \frac{\sum_{ns=1}^{n} \dot{\gamma}^{(\alpha)}}{\sum_{\beta=1}^{N} \sum_{ns=1}^{n} \dot{\gamma}^{(\beta)}} \quad , \tag{16}$$

where n and N are the numbers of grains and slip systems, respectively. Because of the strong cube components in the texture, for visibility purposes, the relative activity of the $(111)[01\bar{1}]$ system, which was the most active slip system in condition 1, is considered representative in further discussion.

The evolution of the relative activities for conditions 1, 2, and 3 is shown in **Fig. 15 (a)**. The relative activity for condition 1 was nearly constant throughout the process. Under conditions 2 and 3, the relative activities rapidly changed immediately after the paths changed and then converged onto that of condition 1, consistent with the transitions of θ. Moreover, it is apparent that the slope of θ changed largely when that of relative activity changed for conditions 2 and 3, confirming the strong correlation between the transitions of θ and the slip activity. In contrast, because no correlation was observed between the transitions of φ and the slip activity, the stress evolution would not be primarily governed by the evolution of the slip activity.

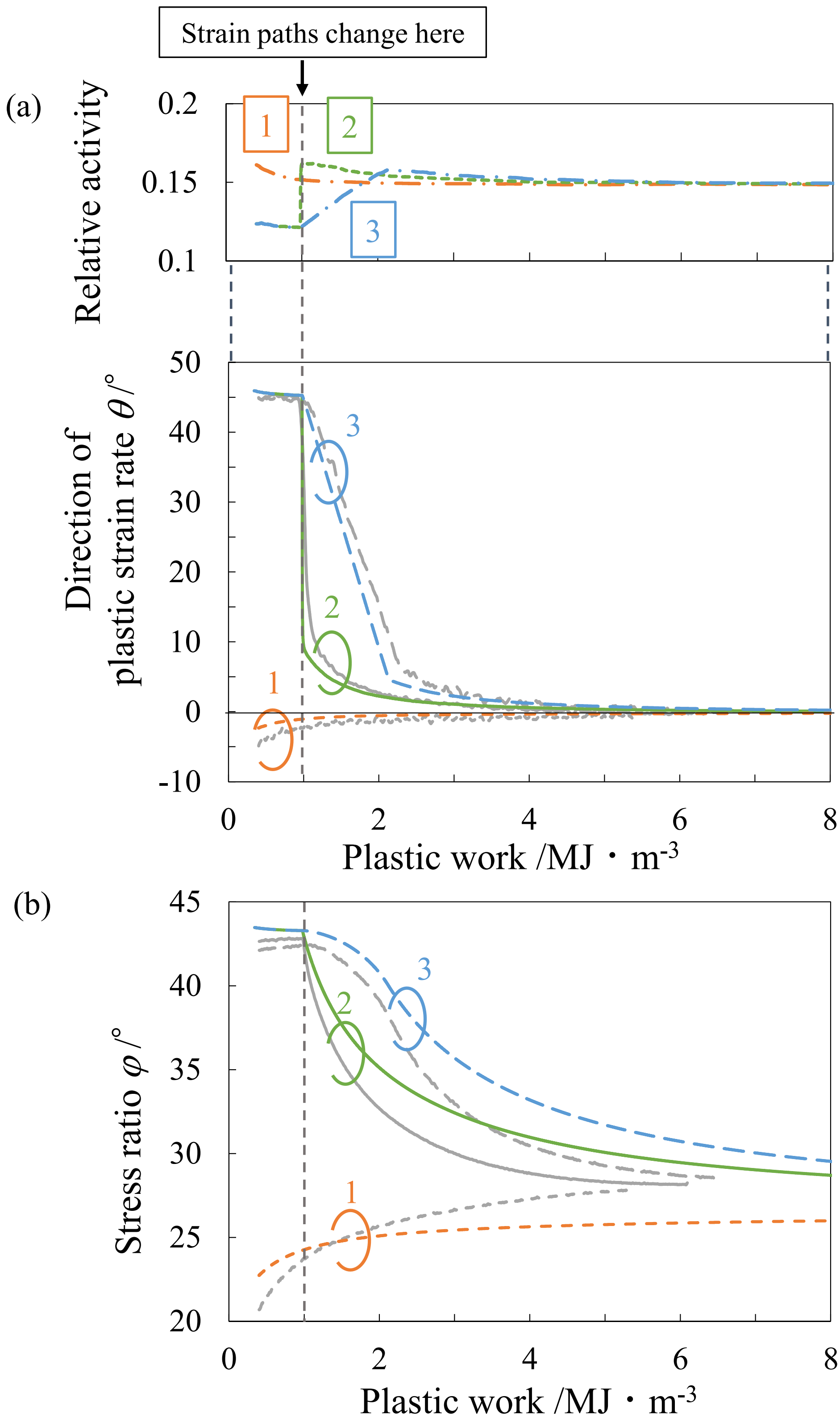

Fig. 15. Crystal plasticity simulation results of transitions of θ (solid lines), φ (broken lines), and relative activity as a function of plastic work for conditions 1, 2, and 3 with a strain-path angle of 0°: the gray solid lines represent the experimental results, and the numbers given to the curves denote the conditions

5.2. Parametric Study

5.2.1 Effect of Strain Rate Sensitivity

The deviation from the experimental results immediately after the strain path change observed in the simulation results was further examined with respect to the mechanical properties of the material. The effect of the strain rate sensitivity on the plastic deformation behavior has often been studied, particularly in terms of the formation of vertices (e.g., Kuroda and Tvergaard, 1999; Kuwabara et al., 2000; Kuroda and Tvergaard, 2001; Kuwabara et al., 2008; Yang and Balan, 2019). For instance, Kuroda and Tvergaard conducted crystal plasticity simulations of abrupt strain-path change tests and showed that larger viscosity yielded less pronounced change in θ just after the path change because the rounded vertex became less sharp, and that subsequent deviations from normality were as large as those obtained with smaller viscosity. Recently, Yang and Balan (2019) showed that the relationship between the direction of viscoplastic strain rate and the stress ratio depended on the strain rate sensitivity: the slope just after the strain-path change became smaller as the strain rate sensitivity increased.

It is clear from Eq. (1) that the evolution of the slip rate $\dot{\gamma}^{(\alpha)}$ strongly depends on the strain rate sensitivity exponent *m*, which was taken to be 0.002 in this study on the basis of experimental results of polycrystalline Al alloy sheets. However, because Eq. (1) modeled the activity of each slip system, it might be more appropriate to use the strain rate sensitivity exponent *m* of single crystals. Lindholm et al. (1965) studied the work-hardening behaviors of single and polycrystalline pure Al under uniaxial tension at different strain rates. According to their results, the rate sensitivity was likely to be larger in single crystals than in polycrystalline materials. A similar tendency was reported for body-centered cubic metals (Takeuchi, 1968). These past studies imply that it would be reasonable to consider that the rate sensitivity exponent at the grain level is different from that at the macroscopic level. Therefore, according to the work by Lindholm et al. (1965), simulations were conducted with larger rate sensitivity exponents as a parametric study.

As examples, **Fig. 16** (a) shows the relationship between φ and θ for condition 2 obtained with $m = 0.002$ (original), 0.044 and 0.2. It is apparent that the slope just after the strain-path change became smaller and the timing at which the slope started decreasing retarded as the strain rate sensitivity increased. These tendencies were consistent with the results reported in the literature (Kuroda and Tvergaard, 1999; Yang and Balan, 2019).

The simulation results for conditions 2 and 3 obtained with $m = 0.044$ and 0.2 are shown in **Figs. 16 (b) and (c)**, respectively**.** The experimental results explained earlier are also shown. When *m* was set to 0.044, the transition of φ for condition 2 was in better agreement with the experimental result than that of $m = 0.002$. In particular, φ tended to converge to approximately 27°, which agreed well with the experimental result and was smaller than that of the result obtained with $m = 0.002$, see Fig. 15 (b). The transition of θ also became closer to the experimental result when *m* was set to 0.044.

(a)

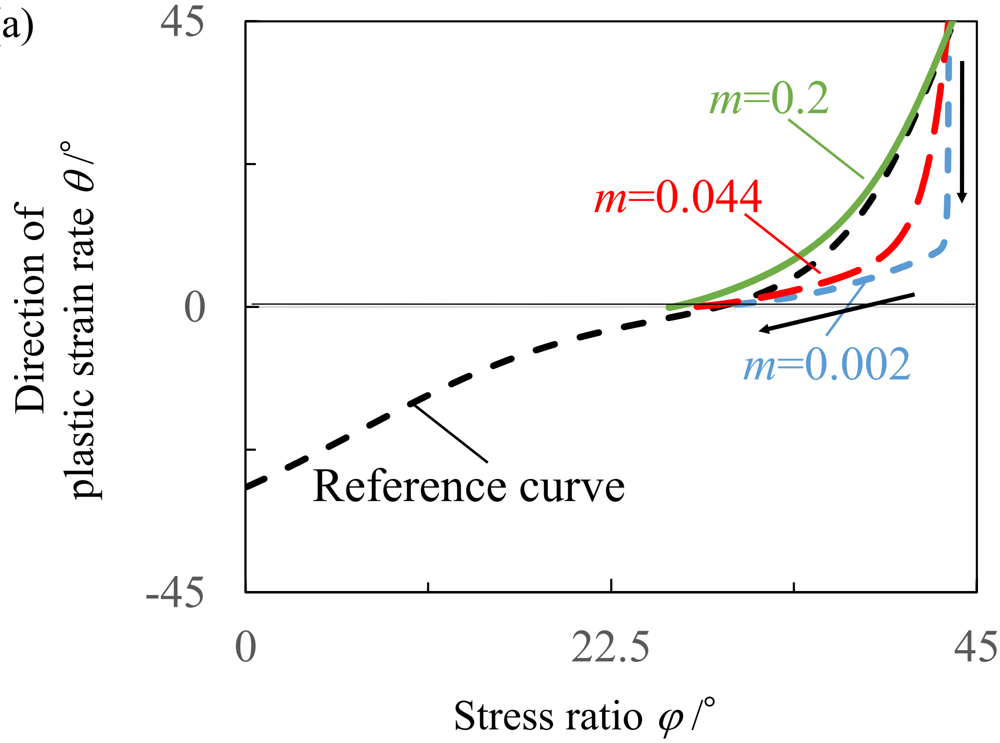

45
0
-45
Direction of
plastic strain rate θ/°
m=0.2
m=0.044
m=0.002
Reference curve
0
22.5
45
Stress ratio φ/°

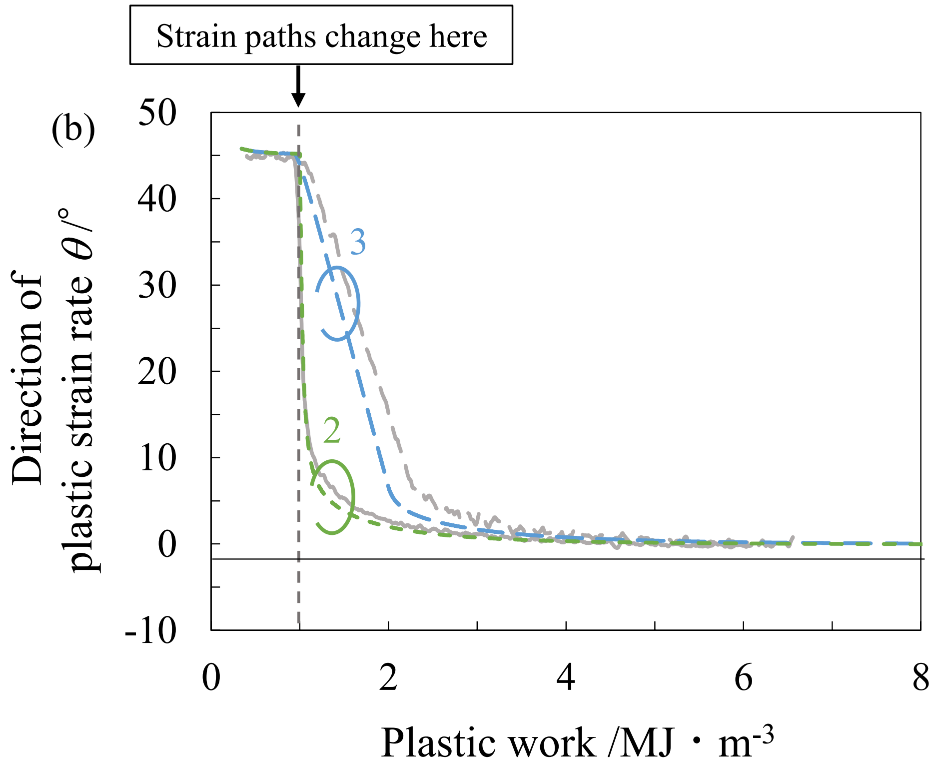
Strain paths change here
(b)
Direction of
plastic strain rate θ/°
50
40
30
20
10
0
-10
3
2
0
2
4
6
8
Plastic work /MJ・m^{-3}

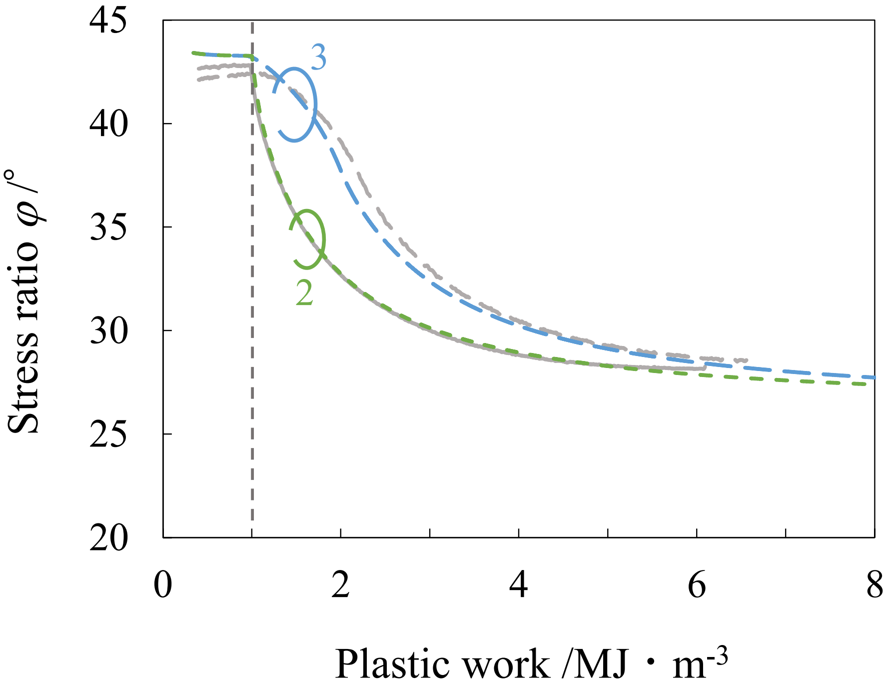
Stress ratio φ/°
45
40
35
30
25
20
3
2
0
2
4
6
8
Plastic work /MJ・m^{-3}

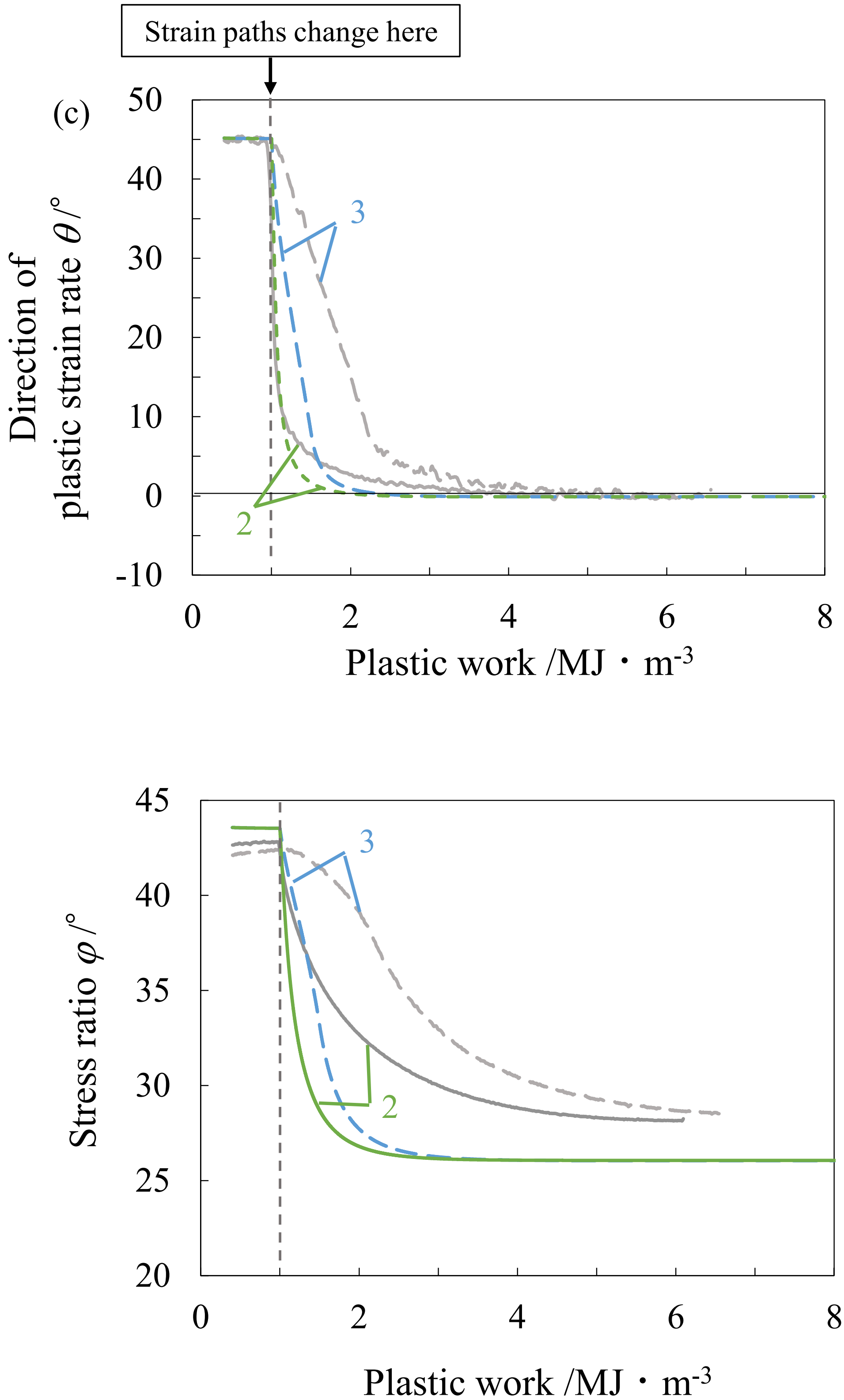

Fig. 16. Crystal plasticity simulation results for condition 2 obtained with different m values: (a) relationships between φ and θ, and transitions of θ and φ as a function of plastic obtained with (b) m = 0.044 and (c) m = 0.2 - In (b) and (c), the gray lines represent the experimental results.

The results of condition 3 also showed better agreements with the experimental results although the evolution of θ still deviated slightly: unlike the results with m = 0.002, the change in φ became sharper in the simulation result than in the experimental result.

When m was set to 0.2, as shown in **Fig. 16(c)**, the change in φ became more sharp than that of m = 0.044 under conditions 2 and 3, and φ tended to converge to a smaller value. Apparently, m = 0.044, which was larger than that determined from the macroscopic stress-strain curves, is more suitable in terms of the evolution of φ and θ. This tendency is consistent with the literature (Kuwabara, et al., 2000).

These results indicate that the transition of φ became more pronounced with an increase in the rate sensitivity exponent, presumably because the evolution of the slip rate $\dot{\gamma}^{(\alpha)}$ after the path change became smoother because of the increase in m. Additionally, the transition of θ was also affected by the rate sensitivity exponent.

In the present results, φ tended to converge to different values depending on the strain rate sensitivity, as explained earlier, whereas θ tended to converge to zero irrespective of the rate sensitivity exponent. In contrast, Yang and Balan (2019) examined the effect of strain rate sensitivity on the deformation behavior after strain-path change without considering work hardening, and showed that the relationship between the viscoplastic strain rate and the stress ratio tended to converge to a certain value irrespective of the strain rate sensitivity. They also reported that the deviation from the reference curve after the strain-path change became more pronounced when isotropic and /or kinematic hardening were considered. Kuroda and Tvergaard (1999) also discussed that the hardening would affect the stress path after the abrupt path change. On the basis of the past studies, the dependence of φ on the strain rate sensitivity observed in Fig. 16 would partially be because of work hardening of the material.

Although m = 0.044 gave the best fits to the experimental results for condition 2 among the values tested in the present case, there is no experimental evidence that m = 0.044 for single crystals is physically appropriate for this material. The appropriate m value would also depend on the other hardening parameters. Modeling of rate sensitivity of this material should be further studied from both macroscopic and mesoscopic viewpoints in future works. Moreover, because the simulation results for condition 3 still deviated slightly from the experimental results even with m = 0.044, it is considered that other mechanisms, including work hardening, caused the difference between the experimental and simulation results.

5.2.2. Strain-Path Change Test for Single Crystal

It has been established that stress and strain distributions are not uniform at the grain level in polycrystalline materials although macroscopically uniform deformation is given (Zhao et al., 2008; Lim et al., 2014; Baudoin et al., 2019). It is likely that the heterogeneous deformation at the grain level disturbs the prompt response of macroscopic stress evolution along with the change in direction of plastic strain rate θ. Kuroda and Tvergaard (1999) performed crystal plasticity simulations of the abrupt strain-path change tests of single crystals and showed that the nonnormality appeared just after the abrupt change, as in the case of polycrystalline materials, indicating that the deviation from the reference curve is inevitable also in single crystals. However, if the heterogeneous deformation at the grain level affected the deviation, it is presumed that the deviation is smaller in single crystals than in polycrystalline materials. To examine the effect of the heterogeneous deformation on the plastic flow, simulations under condition 2 were conducted assuming single crystals where heterogeneity at the grain level would be small. The strain rate sensitivity exponent m was set to 0.044 in this simulation because m = 0.044 gave better agreement with the experimental result, as explained in Section 5.2.1.

An example of the simulation results is shown in **Fig. 17**. The Euler angles in the radians of the single crystal considered here were (4.2191, 2.9200, 5.7445). The results were almost independent of the crystal orientation. Because corresponding experimental results were not available, the reference curve obtained from the Yld2000-2d function determined for the single crystal is shown instead. θ showed sharper changes in the single crystal than in the polycrystalline sheet. In contrast, the transition of φ was somewhat similar to that of the polycrystalline sheet: φ deviated from the reference curve in the plastic work range from W_p = 1.0 to approximately 4.0 MJ · m^{-3}. These results suggest that the effect of the heterogeneous deformation at the grain level is significant on the evolution of θ, while that for the stress evolution was small, indicating that the delay in the stress evolution is almost independent of the number of grains.

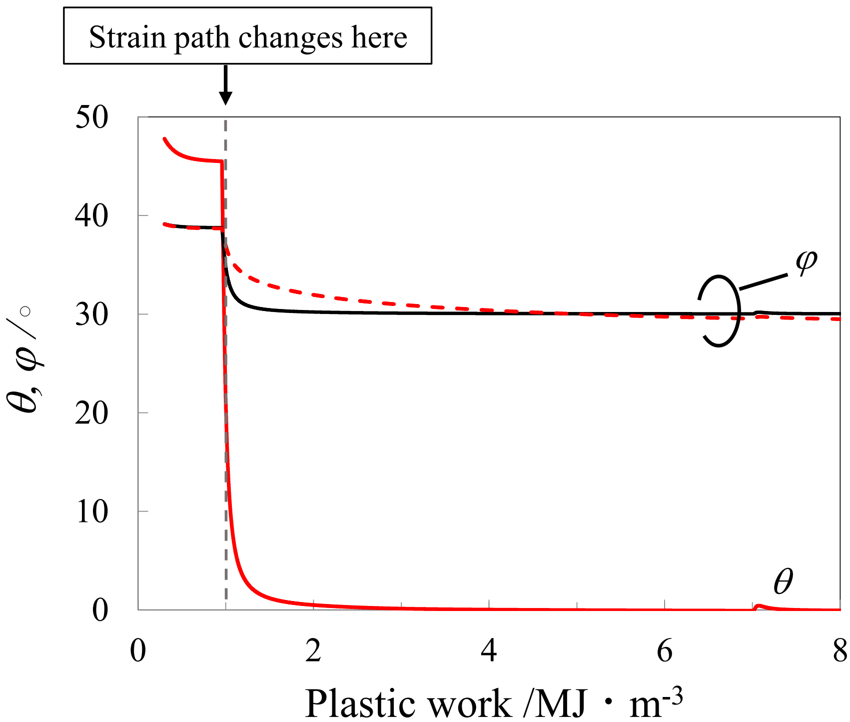

Fig. 17. Crystal plasticity simulation results of transitions of θ (solid line) and φ (broken line) as a function of plastic work for a single crystal: a black solid line is a reference curve of φ obtained from the associated flow rule

5.3. Plastic-Strain-Controlled Test

Considering condition 2 with a strain-path angle of 0°, which corresponds to plane-strain tension in the RD, the plastic strain in the TD could in fact be increased, even after the path change, because total strains, which include elastic strains, were controlled in the test. It is likely that the elastic strains also affect the deformation behavior upon strain path changes, as pointed out by Yang and Balan (2019). Therefore, to examine the effect of elastic strains, a plastic-strain-controlled test was conducted, in which plastic strains ε_{11}^{p} and ε_{22}^{p} were directly controlled instead of total strains. Here, ε_{11}^{p} and ε_{22}^{p} were approximated as follows.

$$\varepsilon_{11}^{p} = \varepsilon_{11} - \frac{\sigma_{11}}{E_{11}} + \nu \frac{\sigma_{22}}{E_{22}}, \tag{17}$$

$$\varepsilon_{22}^{p} = \varepsilon_{22} - \frac{\sigma_{22}}{E_{22}} + \nu \frac{\sigma_{11}}{E_{11}}, \tag{18}$$

where E_{11} and E_{22} denote Young's moduli measured in the uniaxial tensile test along the RD and TD, respectively. The Poisson ratio ν was set to 0.3. Under condition 2, the sheet was stretched equi-biaxially until ε_{11}^{p} and ε_{22}^{p} reached 0.005, followed by an abrupt change to $\tan^{-1}\left(\mathrm{d}\varepsilon_{11}^{p}/\mathrm{d}\varepsilon_{22}^{p}\right)=0^{\circ}$. A crystal-plasticity simulation was also conducted under this condition. The strain rate sensitivity exponent m was set to 0.044 in this simulation.

Fig. 18(a) shows the plastic strain paths achieved in the experiment and simulation. The two results followed the command path overall, but a slight decrease in ε_{22}^{p} occurred immediately after the path change. This indicates that the plastic strains immediately after the path change could not be represented by Eqs. (17) and (18). Therefore, in the following, the deformation behavior immediately after the path change is not discussed, but subsequent transitions are the focus.

Fig. 18(b) shows the transitions of θ and φ for the plastic-strain-controlled test. In the experimental and simulation results, θ decreased suddenly after the path change and overshot to negative values, which corresponded to the slight decrease in ε_{22}^{p}, as shown in **Fig. 18(a)**. Thereafter, θ converged more rapidly in **Fig. 18(b)** as compared with the result of condition 2 (**Fig. 14**). This result suggests that the convergence rate of θ was affected by elastic strains when total strains were controlled. In contrast, the transition of φ still differed from the reference curve calculated from the associated flow rule and was somewhat similar to that of condition 2. This result shows that the tendency of the deviation from the reference curve was affected little by elastic strains.

6. Conclusions

In this study, biaxial tensile tests under various loading paths, including linear strain paths and nonlinear strain paths with abrupt or gradual changes, were conducted using a 6022-T4 Al alloy sheet.

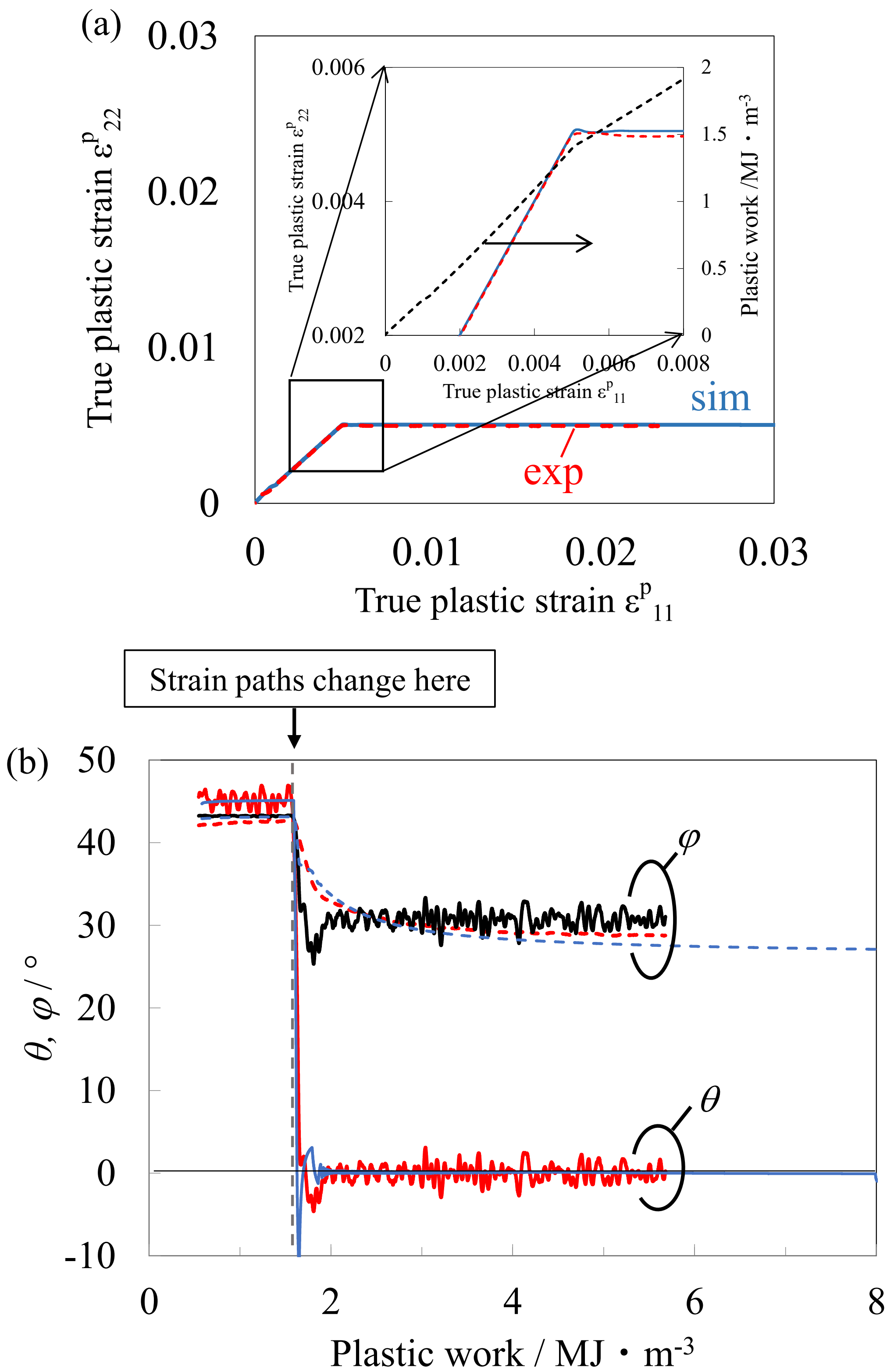

Fig. 18. Results of plastic-strain-controlled test: (a) plastic strain paths and (b) transitions of θ (solid lines) and φ (broken lines) as a function of plastic work — the red and blue curves are the experimental and crystal plasticity simulation results, respectively, and a black solid line in (b) is a reference curve of φ obtained from the associated flow rule

The plastic deformation behavior resulting from strain-path changes was studied in detail, focusing on the transitions of the direction of the plastic strain rate θ and the stress ratio φ during deformation. A cruciform specimen was used for this purpose. Crystal plasticity finite-element simulations were also conducted to investigate the underlying deformation mechanism at mesoscopic viewpoints. The main conclusions obtained in this study are summarized as follows.

1) The evolution of the plastic deformation behavior after strain-path changes is measured experimentally under various strain paths. After the abrupt strain-path change, the plastic work increment of roughly 4.0 $\mathrm{MJ \cdot m^{-3}}$, which corresponds to the strain increment of approximately 0.024 under uniaxial tension in the RD, is necessary until the deformation can be represented again by the associated flow rule with the Yld2000-2d yield function and isotropic hardening assumption. The simulation results reproduce the qualitative tendencies observed in the experiments, but the deviation from the associated flow rule is much more pronounced, particularly under nonlinear strain paths with gradual change.
2) The transitions of θ and φ as a function of plastic work show that both θ and φ tend to converge to certain values regardless of the strain path if the final strain-path angles are identical. It is also found that the relationships between φ and θ temporarily deviate from the associated flow rule immediately after the abrupt path changes because φ cannot follow the rapid change of θ.
3) Parametric studies show that φ tends to converge to different values depending on the strain rate sensitivity, whereas θ tends to converge to a same value irrespective of the rate sensitivity exponent. The rate sensitivity exponent m = 0.044 gives the best fits with the experimental results in terms of the evolution of both θ and φ under an abrupt change path, although the rate sensitivity exponent determined from macroscopic strass-strain curves are m = 0.002. However, the simulation results under a gradual change path still deviated slightly from the experimental results even with m = 0.044, mechanisms other than the rate sensitivity also would affect the predictive accuracy.

Acknowledgments

The help of Mr. Sohei Uchida of the Osaka Research Institute of Industrial Science and Technology is acknowledged for the EBSD measurements. The authors wish to acknowledge Prof. Kengo Yoshida of Shizuoka University for fruitful discussions on the plastic deformation behavior upon strain-path changes. This study was partially supported by the Amada Foundation Grant number AF-2019004-A3 and JSPS KAKENHI Grant number 20H02480. The biaxial tensile experiments were conducted using the apparatus originally developed at the Tokyo University of Agriculture and Technology (Prof. Kuwabara's laboratory), which has now been transferred to Kyoto University. The Al alloy sheet used in this study was provided by Kobe Steel, Ltd.

Appendix

To examine the validities of the finite-element model and the number of crystal orientations used for the present material, a simulation of uniaxial tension along the RD was performed using four different sets of initial crystal orientations extracted from the same result of the EBSD measurement. The pole figures obtained from these sets are shown in Fig. A1. Set 1 corresponded to that used in this work. The overall pole figures and the max intensity values were in good agreements with the experimental results (Fig. 1 (b)). Fig. A2 shows the stress-strain curves and the evolution of *r*-values. The simulation results were almost independent of the set of initial crystal orientations. These results indicate that the finite-element model and the number of crystal orientations used in this work provide sufficiently stabilized results to study the macroscopic deformation behavior of the present material.

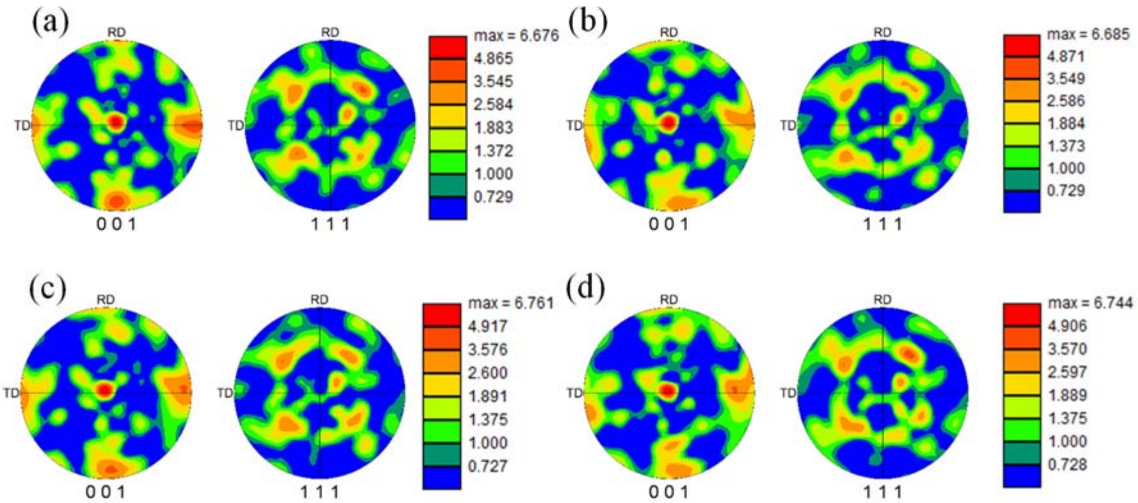

Fig. A1. Pole figures obtained with four different sets of initial orientations: (a) set 1, (b) set 2, (c) set 3, and (d) set 4

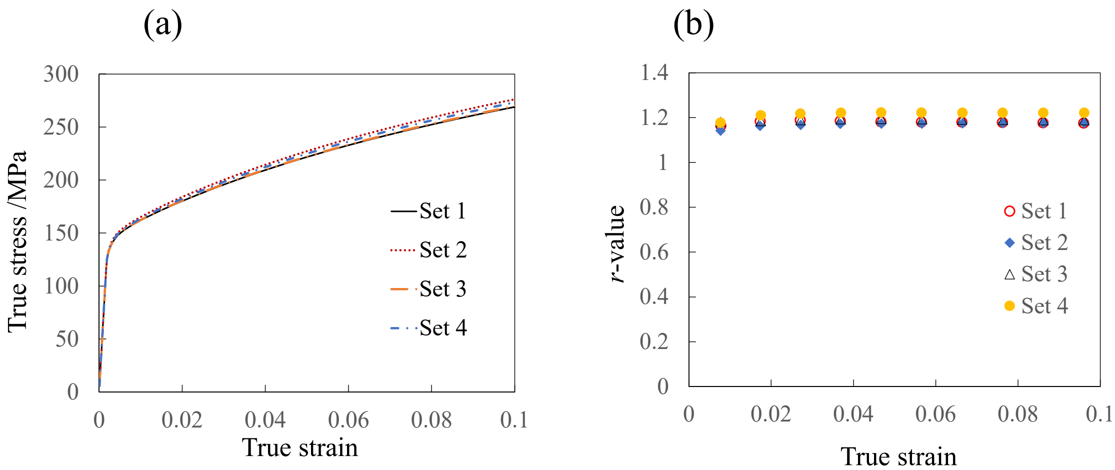

Fig. A2. Uniaxial tensile properties along the RD obtained with four different sets of initial orientations: (a) true-stress–true-strain curves and (b) evolution of the *r*-value

References

Adzima, F., Balan, T., Manach, P.Y., Bonnet, N., Tabourot, L., 2017. Crystal plasticity and phenomenological approaches for the simulation of deformation behavior in thin copper alloy sheets, International Journal of Plasticity 94, 171-191. http://dx.doi.org/10.1016/j.ijplas.2016.06.003

Asaro, R.J., Needleman, A., 1985. Texture development and strain hardening in rate dependent polycrystals. Acta Metallurgica 33, 923-953. https://doi.org/10.1016/0001-6160(85)90188-9

Barlat, F., Brem, J.C., Yoon, J.W., Chung, K., Dick, R.E., Lege, D.J., Pourboghrat, F., Choi, S.-H., Chu, E., 2003. Plane stress yield function for aluminum alloy sheets – part 1: theory. International Journal of Plasticity 19, 1297-1319. https://doi.org/10.1016/S0749-6419(02)00019-0

Barlat, F., Grácio, J.J., Lee, M.-G., Rauch, E.F., and Vincze, G., An alternative to kinematic hardening in classical plasticity, International Journal of Plasticity, 27 (2011), 1309-1327. doi:10.1016/j.ijplas.2011.03.003

Barlat, F., Ha, J., Grácio, J.J., Lee, M.-G., Rauch, E.F., and Vincze, G., Extension of homogenous anisotropic hardening model to cross-loading with latent effects, International Journal of Plasticity, 46(2013), 130-142. http://dx.doi.org/10.1016/j.ijplas.2012.07.002

Baudoin, P., Hama, T., and Takuda, H., Influence of critical resolved shear stress ratios on the response of a commercially pure titanium oligocrystal: crystal plasticity simulations and experiment, International Journal of Plasticity 115(2019), 111-131. https://doi.org/10.1016/j.ijplas.2018.11.013

Cvitanić, V., Vlak, F., Lozina, Ž., 2008. A finite element formulation based on non-associated plasticity for sheet metal forming. International Journal of Plasticity 24, 646–687. https://doi.org/10.1016/j.ijplas.2007.07.003

Feng, Z., Yoon, S-.Y., Choi, J-.H., Barrett, T.J., Zecevic, M., Barlat, F., Knezevic, M., 2020. A comparative study between elasto-plastic self-consistent crystal plasticity and anisotropic yield function with distortional hardening formulations for sheet metal forming. Mechanics of Materials 148, 103442.

Fivel, M., Tabourot, L., Rauch, E., Canova, G., 1998. Identification through mesoscopic simulations of macroscopic parameters of physically based constitutive equations for the plastic behavior of fcc single crystals. Journal de Physique IV, 1-8.

Hama, T., Takuda, H., 2011. Crystal-plasticity finite-element analysis of inelastic behavior during unloading in a magnesium alloy sheet. International Journal of Plasticity 27, 1072-1092. https://doi.org/10.1016/j.ijplas.2010.11.004

Hama, T., Takuda, H., 2012. Crystal Plasticity Finite-Element Simulation of Work-Hardening Behavior in a Magnesium Alloy Sheet under Biaxial Tension. Computational Materials Science 51, 156-164. https://doi.org/10.1016/j.commatsci.2011.07.026

Hama, T., Matsudai, R., Kuchinomachi, Y., Fujimoto, H., and Takuda, H. 2015. Non-linear deformation behavior during unloading in various metal sheets. ISIJ International 55, 1067-1075. https://doi.org/10.2355/isijinternational.55.1067

Hama, T., Kojima, K., Kubo, M., Fujimoto, H., and Takuda, H., 2017. Crystal plasticity finite-element simulation on development of dislocation structures in BCC ferritic single crystals. ISIJ International 57, 866-874. https://doi.org/10.2355/isijinternational.ISIJINT-2017-011

Hama, T., Fujimoto, H., and Takuda, H., 2018. Prediction of differential work-hardening behavior under biaxial tension of steel sheet using crystal plasticity models. Procedia Manufacturing 15, 1808-1815. https://doi.org/10.1016/j.promfg.2018.07.210

Hanabusa, Y., Takizawa, H., Kuwabara, T., 2013. Numerical verification of a biaxial tensile test method using a cruciform specimen. Journal of Materials Processing Technology 213, 961-970. https://doi.org/10.1016/j.jmatprotec.2012.12.007

Hill, R., Hecker, S.S., Stout, M.G., 1994. An investigation of plastic flow and differential work hardening in orthotropic brass tubes under fluid pressure and axial load. International Journal of Solids and Structures 31, 2999-3021. https://doi.org/10.1016/0020-7683(94)90065-5

Hirsch, J., 2011. Aluminium in innovative light-weight car design. Materials Transactions 52, 818-824. https://doi.org/10.2320/matertrans.L-MZ201132

Hutchinson, J.W., 1976. Bounds and self-consistent estimates for creep of polycrystalline materials. Proceedings of the Royal Society of London A 348, 101-127. https://doi.org/10.1098/rspa.1976.0027

Ito, K. 2005. Plastic instability theory and its application to predict sheet metal forming limit. Journal of the Japan Society for Technology of Plasticity 46, 1121-1125. (in Japanese)

Khadyko, M., Dumoulin, S., Cailletaud, G., Hopperstad, O.S., 216. Latent hardening and plastic anisotropy evolution in AA6060 aluminium alloy. International Journal of Plasticity 76, 51-74.

Kuroda, M., Tvergaard, V., 1999. Use of abrupt strain path change for determining subsequent yield surface: illustrations of basic idea. Acta Materialia 47, 3879-3890. https://doi.org/10.1016/S1359-6454(99)00213-X

Kuroda, M., Tvergaard, V., 2001. A phenomenological plasticity model with non-normality effects representing observations in crystal plasticity. Journal of the Mechanics and Physics of Solids 49, 1239–1263. https://doi.org/10.1016/S0022-5096(00)00080-6

Kuwabara, T., Ikeda, S., Kuroda, K., 1998. Measurement and analysis of differential work hardening in cold-rolled steel sheet under biaxial tension. Journal of Materials Processing Technology 80-81,

517-523.
https://doi.org/10.1016/S0924-0136(98)00155-1

Kuwabara, T., Kuroda, M., Tvergaard, V., Nomura, K., 2000. Use of abrupt strain path change for determining subsequent yield surface: experimental study with metal sheets. Acta Materialia 48, 2071-2079.
https://doi.org/10.1016/S1359-6454(00)00048-3

Kuwabara, T., Yoshida, K., Narihara, K., Takahashi, S., 2005. Anisotropic plastic deformation of extruded aluminum alloy tube under axial forces and internal pressure. International Journal of Plasticity 21, 101-117.
https://doi.org/10.1016/j.ijplas.2004.04.006

Kuwabara, T., Horiuchi, Y., 2008. Determining subsequent yield surface of pure titanium sheet by use of abrupt strain path change. International Journal of Material Forming 1, 237-240.
https://doi.org/10.1007/s12289-008-0360-1

Kuwabara, T., Yoshida, K., 2015. Plastic deformation characteristics of light metal sheets -methods of measurement and modeling. Journal of Japan Institute of Light Metals 65, 164-173. (in Japanese)

Kuwabara, T., Mori, T., Asano, M., Hakoyama, T., and Barlat, F., International Journal of Plasticity, 93(2017), 164-186.
http://dx.doi.org/10.1016/j.ijplas.2016.10.002

Lee, E.-H., Stoughton, T.B., Yoon, J.W., 2017. A yield criterion through coupling of quadratic and non-quadratic functions for anisotropic hardening with nonassociated flow rule. International Journal of Plasticity 99, 120–143.
https://doi.org/10.1016/j.ijplas.2017.08.007

Lim, H., Carroll, J., Battaile, C.C., Buchheit, T., Boyce, B., Weinberger, C., 2014. Grain-scale experimental validation of crystal plasticity finite element simulations of tantalum oligocrystals. International Journal of Plasticity 60, 1–18.
https://doi.org/10.1016/j.ijplas.2014.05.004

Lindholm, U.S., Yeakley, L.M., 1965. Dynamic deformation of single and polycrystalline aluminium. Journal of the Mechanics and Physics of Solids 13. 41-53.
https://doi.org/10.1016/0022-5096(65)90030-X

Madec, R., Kubin, L., 2017. Dislocation strengthening in FCC metals and in BCC metals at high temperatures. Acta Materialia 126, 166-173.
https://doi.org/10.1016/j.actamat.2016.12.040

Nemat-Nasser, S., 1999. Averaging theorems in finite deformation plasticity, Mechanics of Materials, 31, 493-523.
https://doi.org/10.1016/S0167-6636(98)00073-8

Ogasawara, Y., Hakoyama, T., Kuwabara, T., Hayamizu, H., Ikeda, T., Takeda, H., and Barlat, F., Procedia Manufacturing, 47(2020), 1270-1273.
10.1016/j.promfg.2020.04.217

Peirce, D., Asaro, R.J., Needleman, A., 1983. Material rate dependence and localized deformation in crystalline solids. Acta Metallurgica 31, 1951-1976. https://doi.org/10.1016/0001-6160(83)90014-7

Phillips, A., Lu, W.-Y., 1984. An experimental investigation of yield surfaces and loading surfaces of pure Aluminum with stress-controlled and strain-controlled paths of loading, Journal of Engineering Materials and Technology 106, 349-354. https://doi.org/10.1115/1.3225729

Safaei, M., Yoon, J.W., De Waele, W., 2014. Study on the definition of equivalent plastic strain under non-associated flow rule for finite element formulation. International Journal of Plasticity 58, 219–238. https://doi.org/10.1016/j.ijplas.2013.09.010

Simmons, G., Wang, H., 1971. Single Crystal Elastic Constants and Calculated Aggregate Properties: A Handbook, Second Edition. MIT Press, Cambridge, Massachusetts, and London, England, 4.

Stoughton, T.B., 2002. A non-associated flow rule for sheet metal forming. International Journal of Plasticity 18, 687–714. https://doi.org/10.1016/S0749-6419(01)00053-5

Stoughton, T.B., Yoon, J.-W., 2004. A pressure-sensitive yield criterion under a non-associated flow rule for sheet metal forming. International Journal of Plasticity 20, 705–731. https://doi.org/10.1016/S0749-6419(03)00079-2

Stoughton, T.B., Yoon, J.W., 2009. Anisotropic hardening and non-associated flow in proportional loading of sheet metals. International Journal of Plasticity 25, 1777–1817. https://doi.org/10.1016/j.ijplas.2009.02.003

Tabourot, L., Fivel, M., Rauch, E., 1997. Generalised constitutive laws for f.c.c. single crystals. Materials Science and Engineering A 234-236, 288-309. https://doi.org/10.1016/S0921-5093(97)00353-5

Tabourot, L., 2001. Vers une vision unifi_ee de la plasticit_e cristalline, Habilitation _a Diriger des Recherches. Univ. Savoie.

Taherizadeh, A., Green, D.E., Ghaei, A., Yoon, J.-W., 2010. A non-associated constitutive model with mixed iso-kinematic hardening for finite element simulation of sheet metal forming. International Journal of Plasticity 26, 288–309. https://doi.org/10.1016/j.ijplas.2009.07.003

Takeuchi, S., 1968. Plasticity of BCC metals. Bulletin of Japan Institute of Metals 7, 14-26. (in Japanese)

Teodosiu, C., Raphanel, J.L., Tabourot, L., 1993. Finite element simulation of the large elastoplastic deformation of multicrystals. Proceedings of the International Seminar MECAMAT’91, 153-168.

Teodosiu, C., 1997. Dislocation modelling of crystalline plasticity. Large Plastic Deformation of Crystalline Aggregates, 21-80.

Tian, H., Brownell, B., Baral, M., Korkolis, Y., 2017. Earing in cup-drawing of anisotropic Al-6022-

T4 sheets. International Journal of Material Forming 10, 329-343. https://doi.org/10.1007/s12289-016-1282-y

Yang, Y., Balan, T., 2019. Prediction of the yield surface evolution and some apparent non-normality effects after abrupt strain-path change using classical plasticity, International Journal of Plasticity, 119, 331-343. https://doi.org/10.1016/j.ijplas.2019.04.006

Yoshida, K., Ishii, A., Tadano, Y., 2014. Work-hardening behavior of polycrystalline aluminum alloy under multiaxial stress paths. International Journal of Plasticity 53, 17-39. https://doi.org/10.1016/j.ijplas.2013.07.003

Yoshida, K., 2017. A plastic flow rule representing corner effects predicted by rate-independent crystal plasticity. International Journal of Solids and Structures 120, 213-225. https://doi.org/10.1016/j.ijsolstr.2017.05.004

Yoshida, K., Tsuchimoto, T., 2018. Plastic flow of thin-walled tubes under nonlinear tension-torsion loading paths and an improved pseudo-corner model. International Journal of Plasticity 104, 214-229. https://doi.org/10.1016/j.ijplas.2018.02.013

Yoshida, K., Okada, N., 2020. Plastic flow behavior of fcc polycrystal subjected to nonlinear loadings over large strain range. International Journal of Plasticity 127, 102639. https://doi.org/10.1016/j.ijplas.2019.12.002

Zecevic, M., Knezevic, M., 2018. Latent hardening within the elasto-plastic self-consistent polycrystal homogenization to enable the prediction of anisotropy of AA6022-T4 sheets. International Journal of Plasticity 105, 141-163. https://doi.org/10.1016/j.ijplas.2018.02.007

Zhao, Z., Ramesh, M., Raabe, D., Cuitino, A., Radovitzky, R., 2008. Investigation of three-dimensional aspects of grain-scale plastic surface deformation of an aluminum oligocrystal. International Journal of Plasticity 24, 2278–2297. https://doi.org/10.1016/j.ijplas.2008.01.002